FEASIBILITY STUDY OF POLARIMETRIC 'SWEAT-SENSING' OF GLUCOSE

By

SEOKKEE MIN

BS, LEHIGH UNIVERSITY, 2013

Thesis

Submitted in partial fulfillment of the requirements for the Degree of Master of Science in the Graduate Program of Biomedical Engineering at Brown University

PROVIDENCE, RHODE ISLAND

MAY 2024

AUTHORIZATION TO LEND AND REPRODUCE THE THESIS

As the sole author of this thesis, I authorize Brown University to lend it to other institutions for the purpose of scholarly research.

Date 25 APR 2024 _____

SEOKKEE MIN, Author

I further authorize Brown University to reproduce this thesis by photocopying or other means, in total or in part, at the request of other institutions or individuals for the purpose of scholarly research.

Date 25 APR 2024 _____

SEOKKEE MIN, Author

This thesis by Seokkee Min is accepted in its present form by the Center of Biomedical Engineering as satisfying the thesis requirements for the degree of Master of Science

Date April 26, 2024 Signature: Jimmy Xu

Dr. JIMMY XU, Advisor

Recommended to the Graduate Council

Date April 26, 2024 Signature:

Dr. KIMANI TOUSSAINT, Reader

Date April 25 2024 Signature: Edith Mathiowitz

Dr. EDITH MATHIOWITZ, Reader

Approved by the Graduate Council

Date April 26 2024 Signature:

Dr. Marissa Gray, Biomedical Engineering

Master's Program Director

Acknowledgements

I would like to thank my wonderful partner, Elizabeth, whose great support allowed me to fully devote myself to my graduate studies. I love and appreciate all that you do and are as a partner.

I also want to thank the Xu lab, especially my advisor Dr. Jimmy Xu and Dr. Petr Moroshkin. Without your help, my foray into the field of optics and photonics would have been entirely difficult and cumbersome as someone with no background in it. I greatly appreciate all your mentorship and guiding of my research development. In addition, I thank the Toussaint lab, especially Dr. Joshua Burrow, who aided me in capturing microscope images for this thesis.

To my family and friends, who have kept me sane during this difficult journey in my graduate studies, I thank you for your moral support.

Lastly, I would like to thank the NASA RI Space Consortium and the US Army DEVCOM, who have partially funded the activities leading to this thesis.

Table of Contents

List of Figures and Tables

Abstract of FEASIBILITY STUDY OF POLARIMETRIC 'SWEAT-SENSING' OF GLUCOSE, by SEOKKEE MIN, ScM, Brown University, MAY 2024.

Blood sugar is an important biomarker in the diagnosis and management of diabetes mellitus. Current sensing methods are invasive, painful, intermittent, and require complex chemical enzyme interactions. An alternative minimally invasive optical sensing method is studied in this work to assess its feasibility and potential. A sub-mm thick optical transmission microfluidic chip utilizing a ferromagnetic core/dielectric shell microfiber array grating was developed for the proof-of-concept polarimetric sensing of an optically active solution (sucrose, as a stand-in for glucose). The tested concentration range was from 0.01 mg/mL to 100.0 mg/mL, which includes the concentration range found in human sweat for glucose in literature. The 50-μm spacing microfiber array microfluidic chip was found to magnify the optical rotation by the sucrose analyte solution by several orders of magnitude within the tested range, over a broad spectral band of a linearly polarized light source with the electrical field oriented orthogonal to the microfibers. The calibration curve of the optical rotation was 0.1428 and 0.1225 degrees per logarithmic concentration (mg/mL) for wavelengths of 1000 and 1200 nm, respectively. Due to the flexibility and scalability of the microfiber and their arrays, the wicking effect of the array and its capability for iontophoresis for sweat generation and extraction, as well as measurement range that covers the concentrations found in sweat, the platform has the potential for enabling many applications, one of which is a wearable sweat sensor of glucose.

Chapter 1: Introduction

1.1 – Diabetes Mellitus and Blood Glucose Measurements

Diabetes mellitus is a chronic disease due to a defect of insulin secretion and/or action, affecting a sizable portion of the world population [1]. The International Diabetes Federation estimates that 537 million adults are living with diabetes, approximately 1 in 10. Diabetes is responsible for 6.7 million deaths, and a 966 billion USD health expenditure in the year 2021. The number of diabetic adults is expected to rise to 643 million by 2030 [2].

Blood Glucose (BG) concentration is an important biomarker used to track and diagnose diabetes. The normal fasting blood glucose range is around 3.9-6.1 mmol/L, or 0.7 - 1.1 mg/mL. However, numerous diabetes patients suffer clinically with persistent hyperglycemia and subsequent complications of the kidney, eyes, and the cardiovascular systems [3]. As such, an accurate, frequent, and long-term monitoring of BG concentration is important in both clinical diagnosis and management of the BG within its normal range for the health outcomes of patients, which can effectively improve life quality, survival rates, and healthcare cost burdens [4].

The most prevalent method of tracking BG is electrochemical sensing via glucose oxidase-coated electrodes. First proposed in 1962 [5], this technique has been very successful in BG detection, including commercial glucose monitoring platforms that sample blood via a finger prick [6]. However, currently available BG sensors such as these have issues, including but not limited to invasiveness, pain, intermittent measurements, and infection risk. In solving these issues, non-invasive optical methods may provide a solution.

1.2 – Sweat Glucose Sensing

Many different optical BG sensors have been proposed, that assess blood, saliva, sweat, interstitial fluid, tear, various tissues, and urine. Detection of glucose in fluids other than blood, such as sweat, provide an effective non-invasive path to estimating BG due to their high correlation [7]. Mechanisms of action of the optical sensors use various physical properties of light, such as polarimetry, colorimetry, coherence, scattering, and the luminescence of fluorescent materials [8]. BG sensors working in the visible/near-infrared (VIS/NIR) typically employ absorbance spectroscopy, but technological bottlenecks such as weak signal, overlapping spectra, and differences in human bodies/dynamic bodily changes make it difficult to accurately extract glucose component information [9]. Several optical polarimetry devices have proposed for extracting glucose information from the aqueous humor of the eye [10] [11], which suffer from noise caused by corneal birefringence in the presence of motion, and can cause visual impairment for the patient. Non-invasive polarimetric blood glucose sensing in general suffers from the weak optical rotation signal of the glucose concentrations involved, confounded with results from skin, a highly absorbing and scattering medium that can completely depolarize light beams [12].

Sweat is produced on the skin. As such, it is an accessible and freely available source of body glucose for interfacing with a measurement device. For optical devices, this means that the results of the glucose signal can be decoupled from the properties of the skin tissue. Even for patients at rest, iontophoresis, the process of passing a weak electrical current through the skin, can be used to generate sweat by skin stimulation [13]. However, a major consideration is that the glucose level in sweat is 0.06-1.11mM (0.01-0.20 mg/mL), which is ~100 times less than the BG levels of 3.9-6.1 mM (0.7 - 1.1 mg/mL) [3], and therefore requires highly sensitive and

accurate sensors. And although there is a time delay of glucose levels between blood and sweat of approximately 8-10 minutes [7], this timescale is short in terms of the length of time in years that chronic glucose dysregulation will cause health complications.

1.3 – Polarimetry

Polarimetry is a measure of different states of polarization, one of which is the optical rotary dispersal of polarized light. When light, an electromagnetic wave, is linearly polarized, its electrical and magnetic field vectors oscillate within their respective planes along the path of its travel (Figure 1). When such a light travels through a solution of an optically active substance, its plane of polarization is found to rotate. Molecules such as glucose, which are chiral and therefore have a break in their spatial symmetry, are optically active and can rotate the polarization of a light passing through its solution (Figure 2). However, maintaining a high degree-of-polarization of light through skin is not possible due to its scattering properties [15]. A sweat sensor allows for the utilization of polarimetry for glucose sensing as no light is required to travel through the skin.

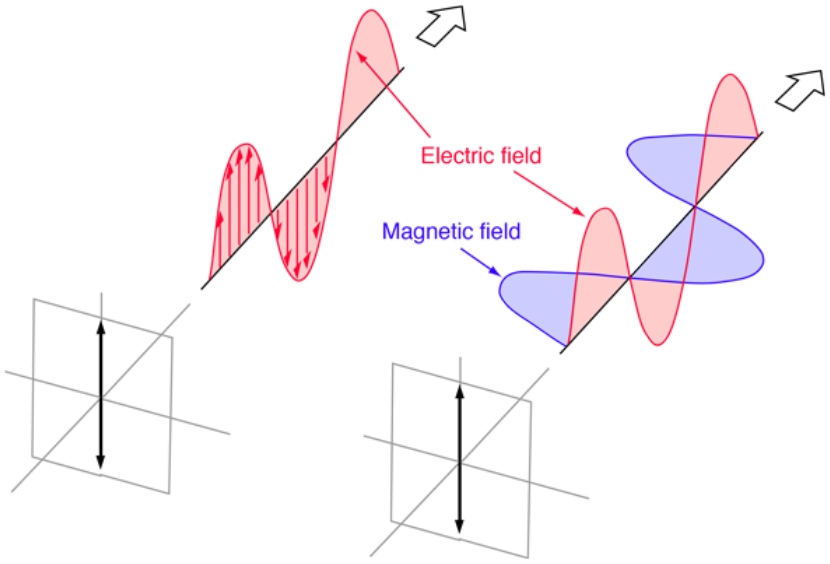

Figure 1: Illustration of linearly polarized light *[16]*.

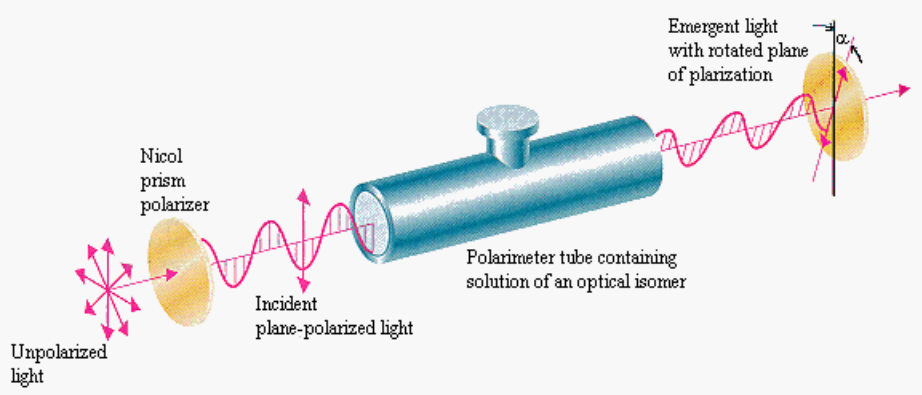

Figure 2: Illustration of polarization rotation due to an optically active solution *[17]*

Every chiral molecule has a known value of specific rotation (α, degrees), which is temperature (T) and wavelength (λ) dependent. Specific rotation has the following relationship with the observed rotation (θ, degrees), concentration (C, g/mL), and path length (L, dm):

$$[\alpha]_{\lambda}^{T}\ (molecule) = \frac{\theta_{observed}}{C * L}$$

D-(+)-Glucose, the chiral isomeric form of glucose used by the body, has a specific rotation of +52.2° in a 20 °C water solution in the visible/near-infrared (VIS/NIR) wavelength range [18]. For the low concentrations required for sweat sensing, as well as the limitations on path length for the size of a wearable device, polarimetry presents a challenge.

For the purposes of this study, sucrose (also known as table sugar) has been utilized due to its ready availability. Sucrose is a disaccharide, composed of both glucose and fructose subunits. For human consumption, both glucose and sucrose are of the D- (dextrorotary) chiral form, meaning that they both rotate polarization in the same direction. Sucrose has a specific rotation of approximately +66.5° in the VIS/NIR range, not too dissimilar to glucose [18]. The chemical formula/diagram of glucose and sucrose can be found in Figure 3 below.

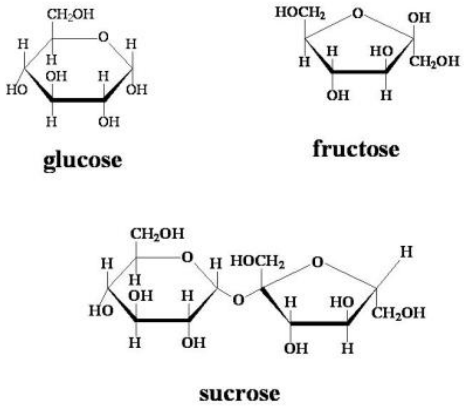

Figure 3: Chemical diagrams of sucrose, fructose, and sucrose *[19]*

1.4 – Photonic Crystals

Photonic crystals are structured materials, with periodic arrangements of changing refractive indices, used in numerous areas of study to manipulate electromagnetic waves. The properties arise from both the constituent material properties as well as their geometrical structure [20], which can be further tuned by or sense changes in temperature, strain, chemical parameters, and the presence of chemical or biological elements [21]. For example, the change in refractive index of an analyte solution on a photonic crystal can change the characteristics of that system, such as wavelength and polarization dependent absorption and scatter. Such methods have been utilized in sucrose concentration sensing, utilizing the resonance features of a one-dimensional photonic crystal waveguide [22]. Other examples of photonic crystals include optical fiber gratings, high- and low-reflective coatings, surface plasmon resonance devices, and more [23].

Ferromagnetic materials are an interesting contender for optical crystals, as they tend to have stronger magnetic responses and higher potential for wave absorption compared to

paramagnetic materials [24]. As chiral molecules can become spin-polarized near magnetic surfaces, meaning that electrons with a particular spin will accumulate at one end of the molecule, the molecules will align themselves in a particular orientation on that surface. This method has been used to separate different enantiomers, or different chiral forms of the same molecule, using a magnet [25]. With the combination of the potential for electromagnetic wave interactions, as well as the orientation alignment of chiral molecules onto its surface, the addition of ferromagnetic materials within photonic crystals that can create resonances for certain frequencies of waves presents an interesting potential for concentration sensing of optically active substances.

1.5 – Experimental Aim

The aim of this research is to evaluate the feasibility of an optical method of sucrose sensing (as a stand-in for glucose) in a platform that is compatible with wearability and sweat extraction and transport. This goal is a continuation of my previous work with a ferro-magnetic/dielectric core-shell microfiber and creating arrays to tune their reflectance characteristics within the VIS/NIR range. This core-shell wire array demonstrated a wavelength dependent reflection, which was polarization dependent (with the electrical field orthogonal or parallel to the wires), as well as an optical cavity effect [26]. With the addition of a refractive index change due to the sucrose solution as well as the possible orientation of the chiral molecules to the ferromagnetic surface, I hypothesized the potential for utilizing the platform as an optical molecule sensor. To simplify the study, by disregarding the polarization and angle dependent reflectance of the system, I chose to study only the transmission characteristics of the microfiber array at an orthogonal angle of incidence. The underlying mechanisms are however equally applicable to the reflection counterpart.

The microfibers also readily lend themselves to a wearable sweat sensor. As the cores are conductive, the array itself can be utilized for iontophoresis to harvest sweat. Inductive and resistive heating options are available as well, due to the ferromagnetic and resistive properties of the alloy, to induce sweat via temperature as well as actively tuning the optical characteristics of the array. The borosilicate shell protects the alloy core, rendering the fibers chemically inert and mechanically durable. As the microfibers are thin, they are flexible even with the low strain rate of the materials themselves and therefore can conform to the curvatures of the human body. In addition, the thin channels formed by the microfibers in an array can readily wick fluid due to capillary forces, which theoretically increase as the array spacing decreases.

Chapter 2: Methods

2.1 – Fiber Array Fabrication.

The CoFeSiB ferromagnetic alloy core and borosilicate glass dielectric shell microfibers used for this study were created by a former member of the lab (Dr. Chen Zheng). The microfibers used have a core and an outer diameter of 20 and 27 μm, respectively, and were laid in an array on a substrate of a double-sided adhesive plastic sheet (300LSE Double-sided Adhesive, 3M), using a custom designed and fabricated fiber winder. Two different wire array spacings were utilized for this study: 50 μm and 100 μm, center-to-center spacing.

The adhesive plastic is composed of a polyethylene terephthalate (PETE) backing, with an acrylic-based adhesive. The fiber winder was fabricated using various off-the-shelf components, as well as custom ones designed and fabricated via laser-cutting, CNC machining, press-fitting, and 3D printing (Figure 4). The controlled winding is enabled by employing two micro-controlled planetary-geared (27:1) stepper motors (17HS13-0404S-PG27C, Osmtec): one

controls the winding drum/roller rotation for the winding motion, and the other controls the linear stage (leadscrew actuated: M8x1.5 thread) for controlling the spacing between the windings. The winding drum is 76.2 mm in diameter, CNC machined from high molecular weight polyethylene. A micro-step of the linear stage motor is equivalent to a theoretical winding separation of 1.085 nm, which was chosen to reliably target the desired winding spacing which is 4+ magnitudes larger. The control schema was coded in Python3, which drives the motors at 60 kHz to maximize winding speed while avoiding the fundamental frequency of the microfiber wire. The winding process as well as sample images are shown below in Figure 5.

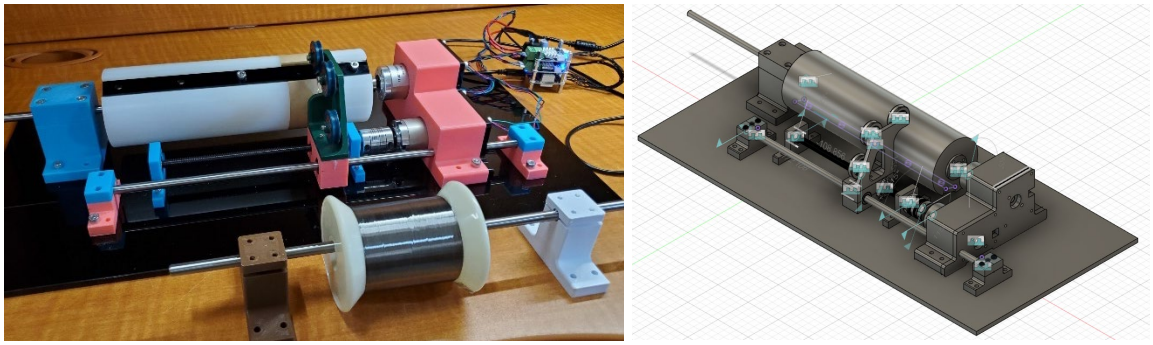

Figure 4: [Left] Prototype fiber winder, with a 76.2 mm winding drum/roller, and theoretical 1.085 nm minimum winding separation step size. [Right] CAD model of the winding setup.

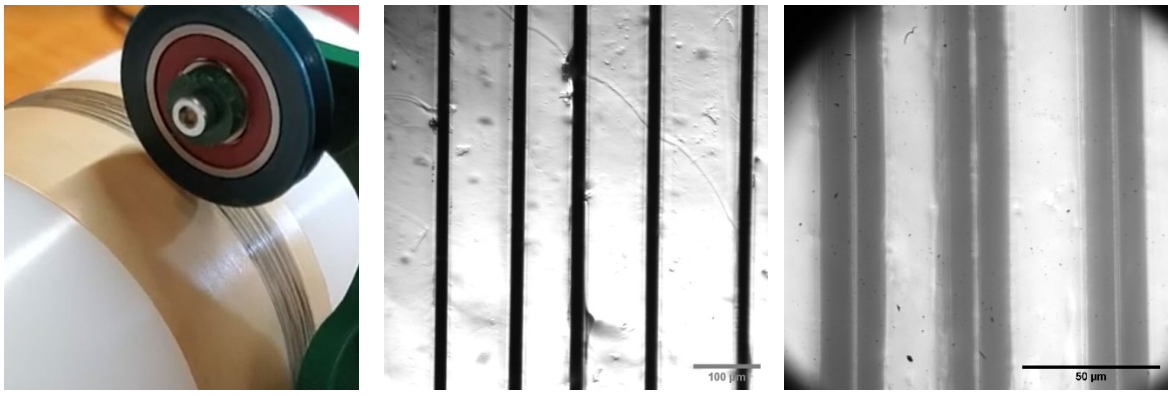

Figure 5: [Left] the winding in progress on a 3M PETE adhesive substrate. The light optical microscopic images of a 100-µm [Center] and 50-µm [Right] center-to-center spaced wire array.

2.2 – Microfluidic Chip Fabrication

The microfluidic chips were fabricated using a microscope slide (Premiere, C&A Scientific) as a substrate to ensure flatness. The sample array, mounted on the PETE adhesive sheet, was adhered to the microscope slide, such that the wires were facing up and away from the microscope slide. A 500-µm shim (Shim Stock, Artus Corporation) was added onto the PETE sheet adjacent to the wire array, such that a channel formed above the wires. A blunt precision tip needle (26 G, Becton Dickinson) was added as a fill port to the microfluidic channel, and a second PETE adhesive sheet was laid over the shim, to cover the channel area. The joints were further sealed with a cyanoacrylate adhesive. The cross-sectional schematic of the fluidic channel and a picture of the microfluidic chip are shown in Figure 6 and Figure 7, respectively. The control sample was fabricated in the same manner, except that a PETE adhesive sheet without any mounted wire arrays was used for the fluidic channel.

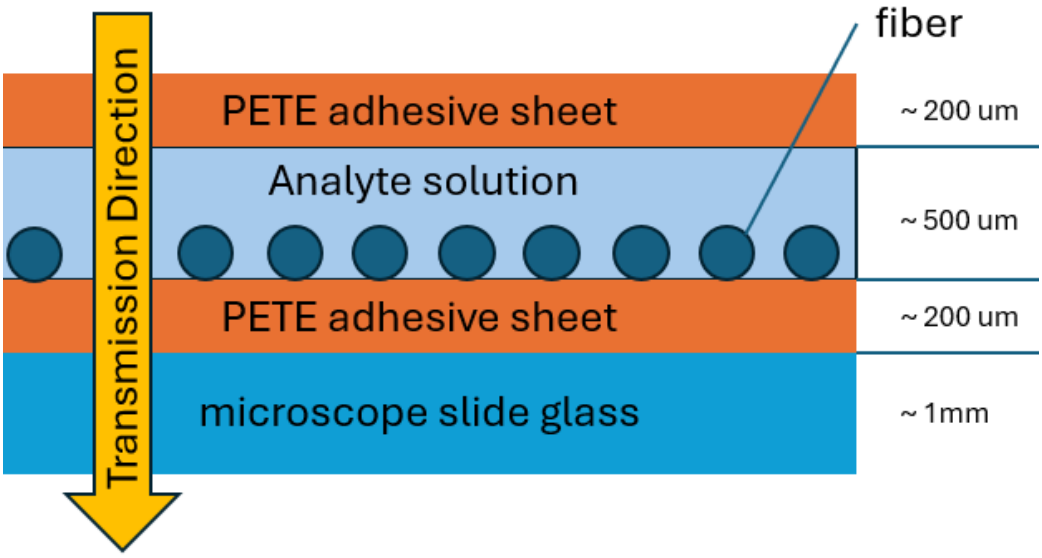

Figure 6: Cross-sectional schematic of the microfluidic chip.

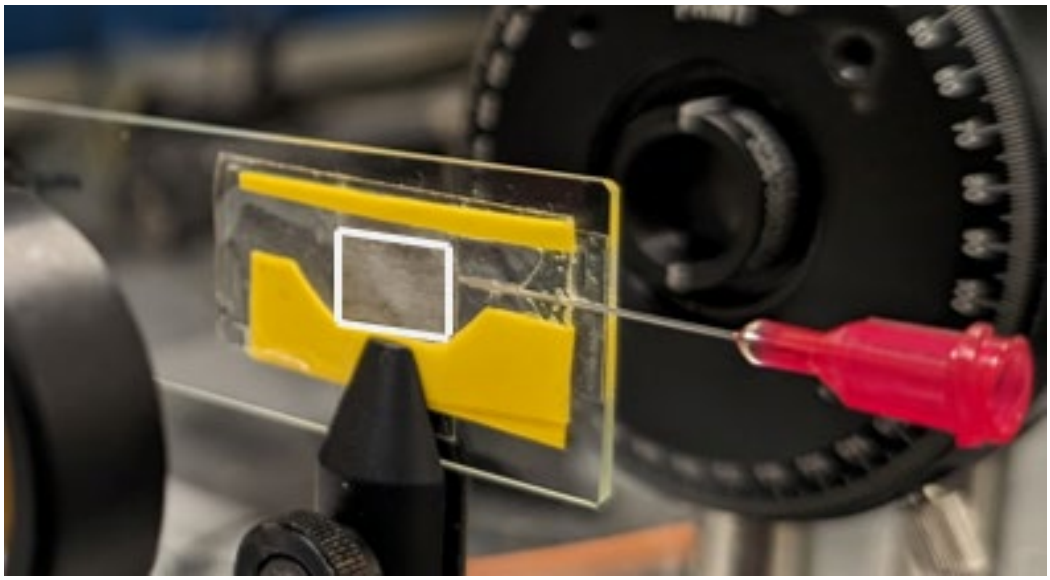

Figure 7: The microfluidic chip sample, mounted in the testing setup. Wire array area is highlighted with a white box. The yellow plastic is the 500-µm shim.

2.3 – Fluid Wicking Testing

For demonstrating the wicking ability of the microfluidic channel, a microfluidic chip sample with the 50-µm array approximately 1 cm wide was created in the same way as mentioned above, except for a fill port needle. In addition, both ends of the wire arrays were open and accessible. A red food-dye solution of deionized (DI) water was dropped onto one end of the chip, with a tissue paper on the other end to function as visual indicators of the wicking properties of the wire array microfluidic channel.

2.4 – Optical Transmission Testing

A broad spectra halogen source (OSL2 Fiber Illuminator, Thorlabs) was coupled into a multimodal optical fiber (M74L02 - Ø400 µm, 0.39 NA, Low OH, FC/PC-FC/PC Fiber Patch Cable, Thorlabs), collimated (F220SMA-1064, Thorlabs), and linearly polarized using a broad-

spectrum polarizer centered at a wavelength of 1 µm (LPNIR050-MP2, Thorlabs) mounted on a rotational stage. Two different source polarizations were used for this study: the E-field parallel ($E_{\parallel}$) and orthogonal ($E_{\perp}$) to the direction of the wires in the array (Figure 8). The linearly polarized light was then focused using a lens (5 cm focal length, Thorlabs) onto the microfluidic chip at a normal angle of incidence. The resulting output light along the transmission axis (centered at the zeroth order diffraction for the wire array) was then filtered using a second linear polarizer analyzer ((LPNIR050-MP2, Thorlabs) mounted on a rotational stage, to capture the co- and cross-polarization components. The resulting light was coupled into a multi-modal optical fiber via a collimator and measured using a spectrometer (AQ6317 Optical Spectrum Analyzer, Ando, Japan), which measures the power of the input light at each resolution wavelength. The spectrometer was operated via a custom LabVIEW program. The measurement range included wavelengths of 600 nm ~ 1700 nm, with a spectral resolution of 1 nm. The optical experimental setup is shown in Figure 9. The direction of the optical transmission across the microfluidic chip is shown in Figure 6.

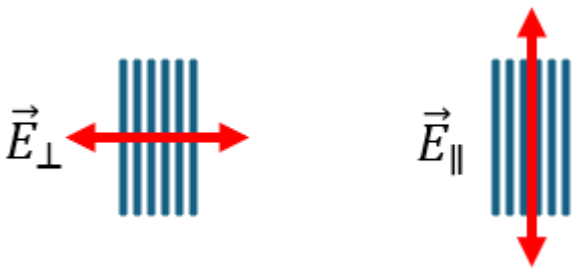

Figure 8: The source polarization orientations w.r.t. the direction of the wires. The E-field polarization orthogonal to the wires is shown on the left, and the E-field polarization parallel to the wires is shown on the right.

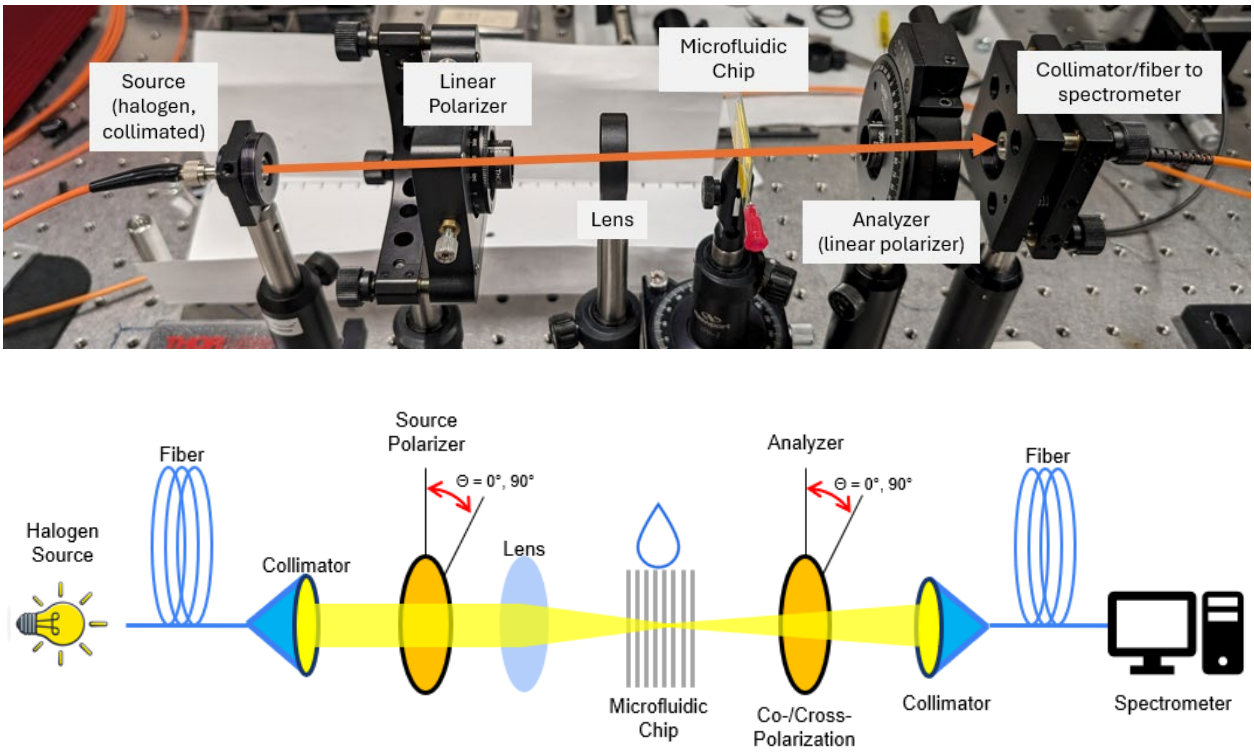

Figure 9: [Top] A picture of the optical experimental setup. Each component is labeled. The optical path is shown via the red arrow. [Bottom] A schematic of the experimental setup.

Various concentrations of sucrose (≥99.5%, Sigma Aldrich) solutions were made as an analyte solution and pumped into the microfluidic channel chamber using the fill port for optical measurement. DI water was used for all experiments. All sucrose weight measurements were performed via an electronic balance (BCE124-1S Entris II Analytical Balance, Sartorius) and all DI water measurements were made using a graduated cylinder. All microfluidic chip samples (control, 50-µm and 100-µm arrays) were evaluated using four different concentration solutions: 0.000 mg/mL (DI water), 0.01 mg/mL, 1.00 mg/mL, and 100.0 mg/mL. The 50-µm microfiber array was further evaluated at 0.10 mg/mL and 10.0 mg/mL concentrations, to gain a higher resolution dataset. The measurements were performed from the least to the most concentrated to not confound results due to residual sucrose within the microfluidic channel. Each filling cycle

used 1 mL of solution to flush out the previous analyte solution. All measurements, for each microfluidic chip sample and analyte concentration included replicates for statistical analysis (N = 3).

The spectra of the source were also measured without the microfluidic chip within the line of the optical path axis, at both co- and cross- polarizations, for use in calculating the normalized transmittance/extinction of the microfluidic chip with the different analyte solution concentrations.

2.5 – Data Analysis

The spectra of each experiment were processed and analyzed via Python3 using a Jupyter Lab Notebook environment. The polarization rotation (θ) was calculated by taking the inverse-tangent of the ratio of the power of the cross-polarized spectra ($P_{\perp pol}$) over the co-polarized spectra ($P_{\parallel pol}$). The rotation was converted from radians to degrees (Equation **1**). The total spectra were calculated by taking the square root of the sum of the squares of each polarization component (Equation **2**).

Equation 1: $$\theta = \frac{180^\circ}{\pi} * arctan\left(P_{\perp pol} / P_{\parallel pol}\right)$$

Equation 2: $$P_{total} = \sqrt{{P_{\perp pol}}^2 + {P_{\parallel pol}}^2}$$

In order to remove any alignment issues of the wire array with respect to the source polarization, as well as any confounding material effects, the net polarization rotation of the analyte solution was calculated by subtracting the rotation spectra of the DI water from all the other samples. The calibration curves at specific wavelengths were created by taking the average

rotation of each sample at a wavelength and plotting the value against the concentration of the analyte solution.

The "net optical rotation" was also calculated, by subtracting the rotational spectra of the 0.000 mg/mL (DI water) data from all the other rotational spectra, for each microfluidic chip sample. This was done to remove any polarization rotation contributions due to the prototyping materials (i.e., strain induced birefringence of the polymer sheets), and any alignment issues between the source polarization and the microfiber array.

The theoretical optical rotation for sucrose solutions of the concentrations used for this study were also calculated via Equation 3. The observed optical rotation ($\theta_{theoretical}$) is a product of the specific rotation of sucrose ($\alpha_{sucrose}$, in degrees), the path length (L, in decimeters), and the concentration of the solution (c, in g/mL).

Equation 3: $$\theta_{theoretical} = \alpha_{sucrose} * L * c$$

Chapter 3: Results

3.1 – Optical Rotation

The control and 100-µm array microfluidic chips demonstrated similar behavior, where the optical rotation was nearly 90° for wavelengths between 600~1000 nm, which gradually tapered down to approximately 55° as the wavelength increased until 1700 nm. This large optical rotation is most likely an effect of the PETE adhesive layer, as a contribution of stress-induced birefringence due to the residual stresses of the manufacturing process [27]. Also, the separation in rotation due to the concentration of the analyte solution is low compared to the dynamic range of the rotation amounts for both sets of data. However, the control data appears to have little difference in optical rotation compared to the 100-µm array, especially in the higher wavelength range. When the source polarization is parallel to the wires (Figure 10) compared to orthogonal

(Figure 11), the rotation appears to be grouped much tighter, especially for wavelengths above 1200 nm.

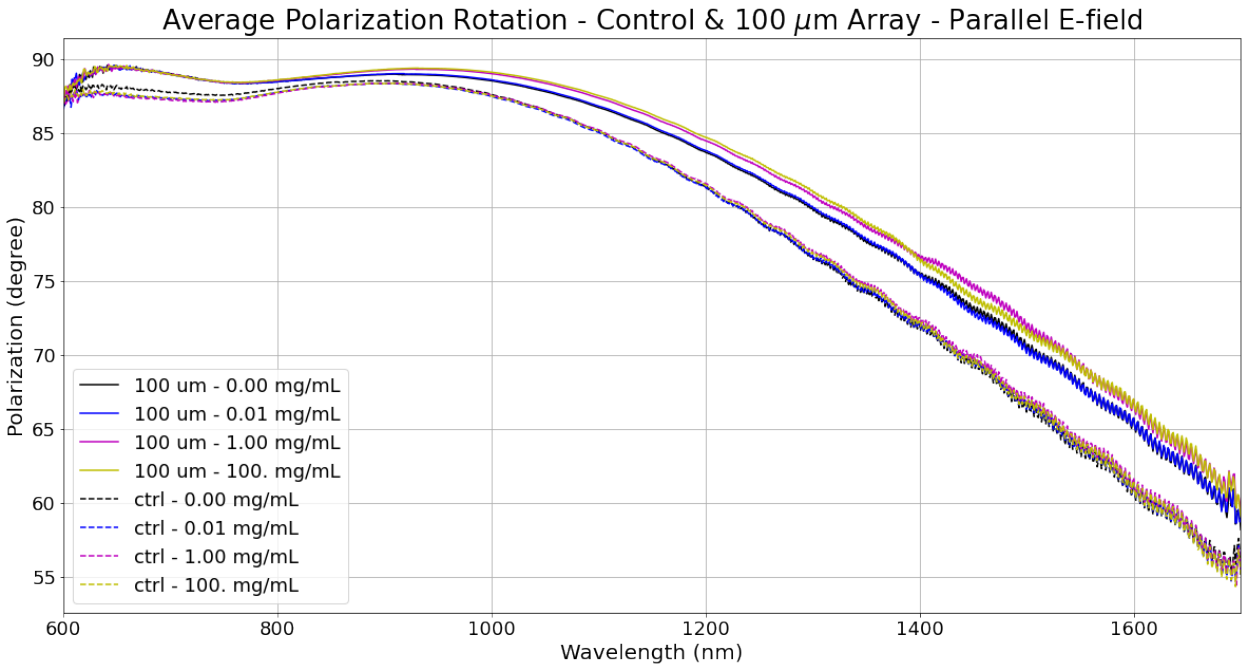

Figure 10: The average optical rotation spectra of the control (dashed) and 100-µm array (solid) microfluidic chips, for a parallel E-field source.

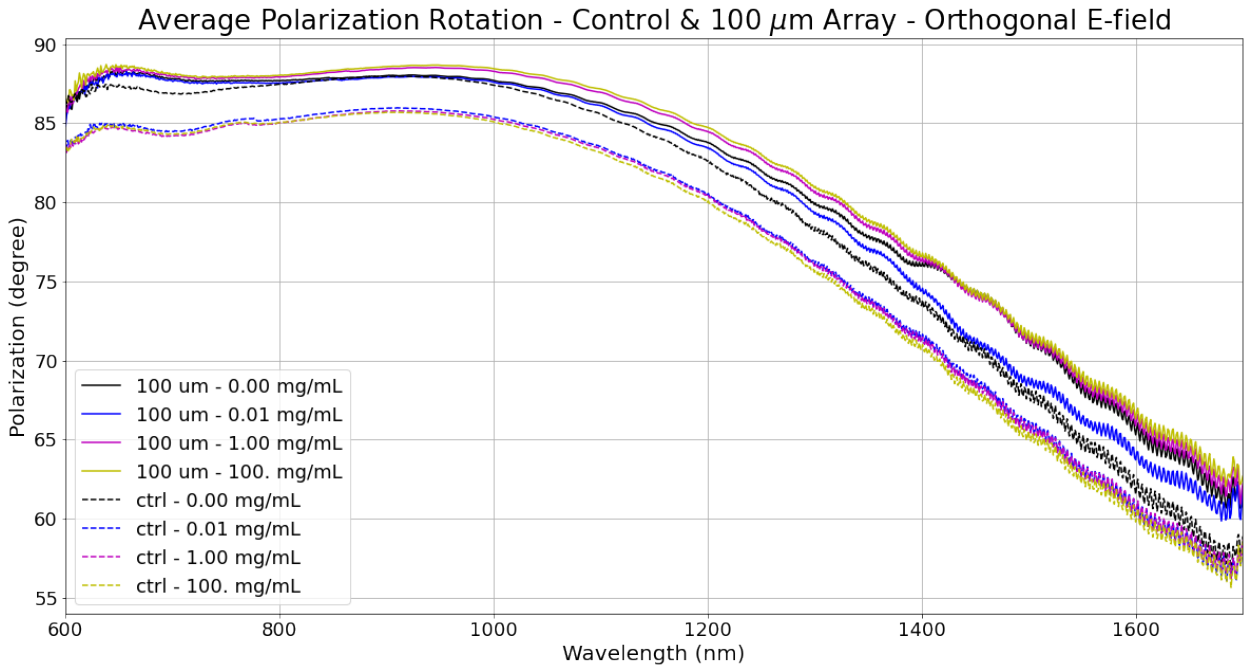

Figure 11: The average optical rotation spectra of the control (dashed) and 100-µm array (solid) microfluidic chips, for an orthogonal E-field source.

The net average optical rotation for the control sample appears to be grouped per polarization orientation (Figure 12). The case of parallel polarization presents positive optical rotation, with the relationship not being monotonically increasing with an increase in the analyte concentration. In the case of orthogonal polarization, a negative rotation is observed that monotonically decreases as concentration increases. However, the method for calculating the optical rotation (Equation 1) is insensitive to rotations above 90° as the phase of the electrical field is unknown, and the results would be mirrored for rotations from 0° to 90°, and from 90° to 180°. Combined with the flipped dependence on concentration, it is most likely that the negative rotation is an artifact of the methodology.

A closer look at wavelengths of 1000 nm and 1450 nm (Figure 13) show that the large standard error of the optical rotation curves, meaning that the rotation due to the different tested

concentrations cannot be determined from each other, even with the monotonic relationship. As such, the control sample shows no strong correlation between the optical rotation amount and the concentration of the analyte solution.

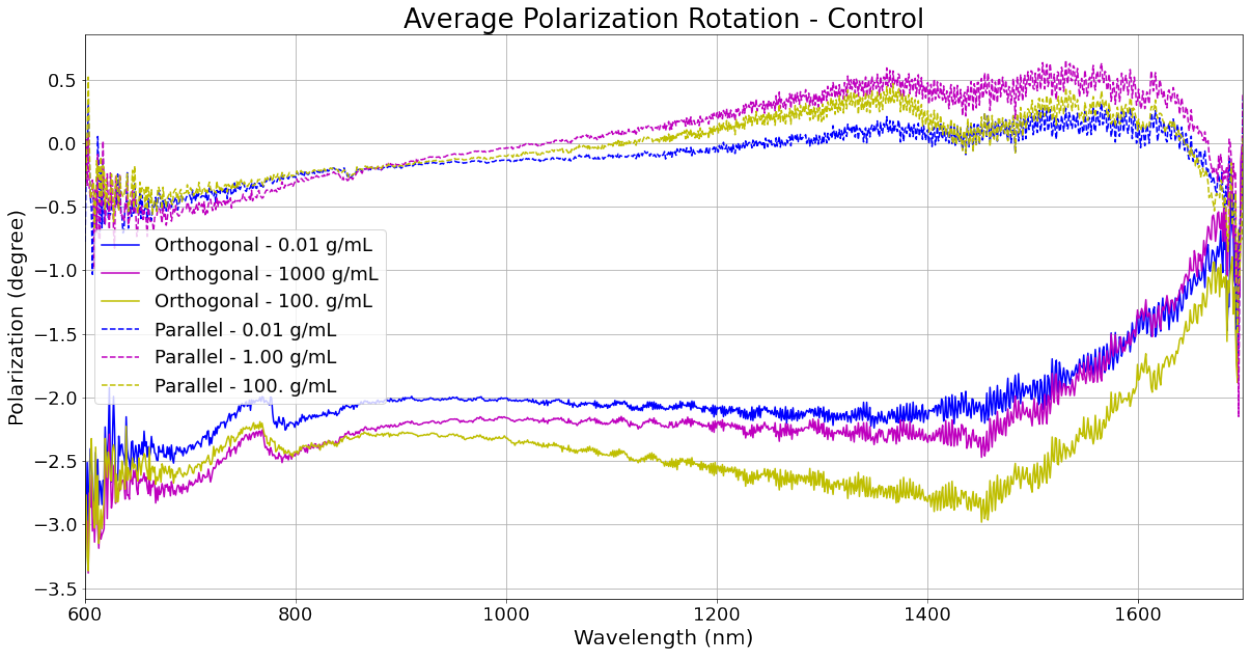

Figure 12: Average net optical rotation for the control sample. The solid and dashed lines represent an E-field direction orthogonal and parallel to the wires, respectively.

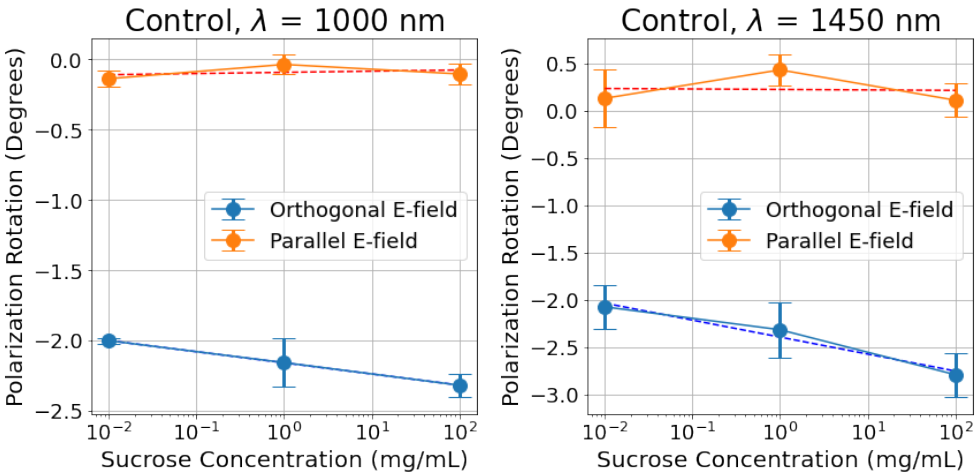

Figure 13: Average optical rotation of the control sample with standard error bars, plotted as a function of analyte concentration, at wavelengths of 1000 nm [left] and 1450 nm [right].

The net average optical rotation for the 100-µm array falls within a similar range and increases monotonically as a function of analyte concentration for both the orthogonal and parallel polarizations (Figure 14). In the case of the orthogonal polarization orientation, the net optical rotation of the 0.01 mg/mL sucrose solution is mostly negative, meaning that it is less than the optical rotation of DI water. It is unclear whether this is real or a test artifact but brings into question whether the results observed for the 100-µm is solely due to the optical rotation effect of the sucrose. In addition, the large error for the 100.0 mg/mL concentration makes it indistinguishable from the 1.00 mg/mL concentration, making this sample unreliable for this analyte concentration range.

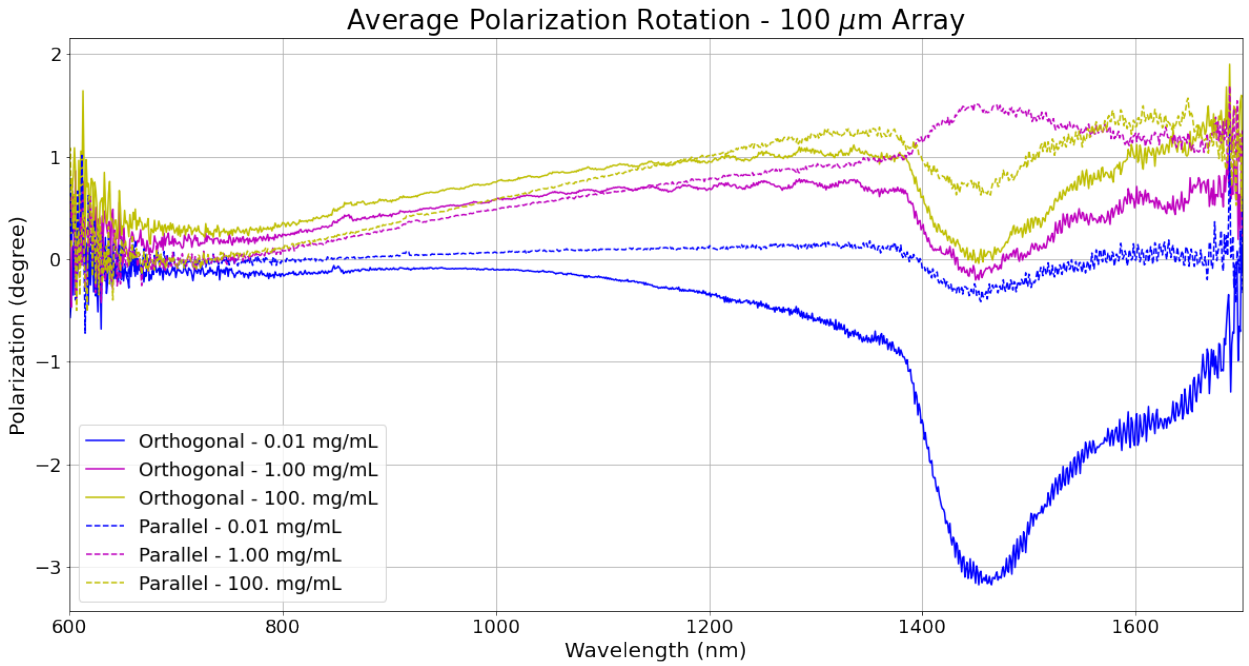

Figure 14: Average net optical rotation for the 100-µm array sample. The solid and dashed lines represent an E-field orthogonal and parallel to the wires, respectively.

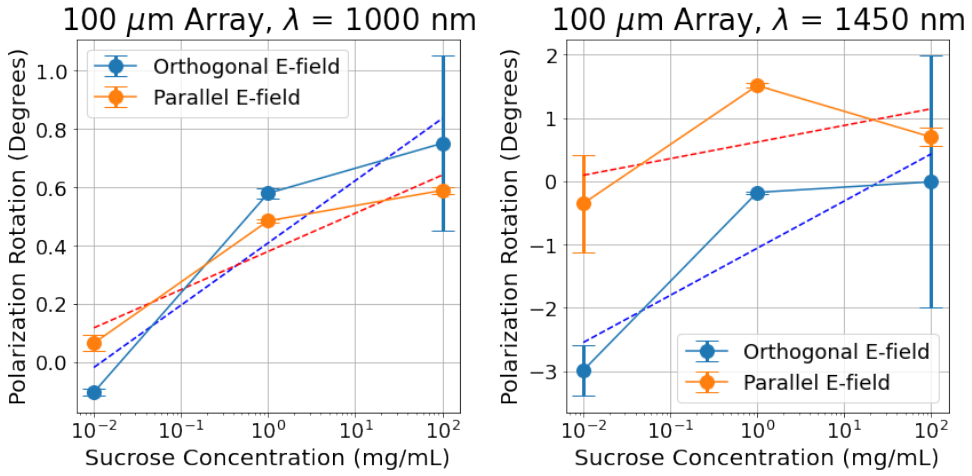

Figure 15: Average optical rotation of the 100-µm array sample with standard error bars, plotted as a function of analyte concentration, at wavelengths of 1000 nm [left] and 1450 nm [right].

The spectra of the 50-µm spacing array (Figure 16) in contrast displayed much less optical rotation, generally under 4° (compared to almost 90° for the control and 100-µm array), and much less variation overall, producing regions of relatively flat rotation amounts over

several hundred nm in wavelength. The degree of optical rotation is clustered for the case where the polarization is parallel to the wires, in comparison to the orthogonal polarization case, where all the rotation spectra curves are clearly separated for all analyte concentrations. The optical rotation monotonically increases as a function of the sucrose concentration in the case of the orthogonal polarization, for the wavelength range of approximately 850 nm to 1350 nm.

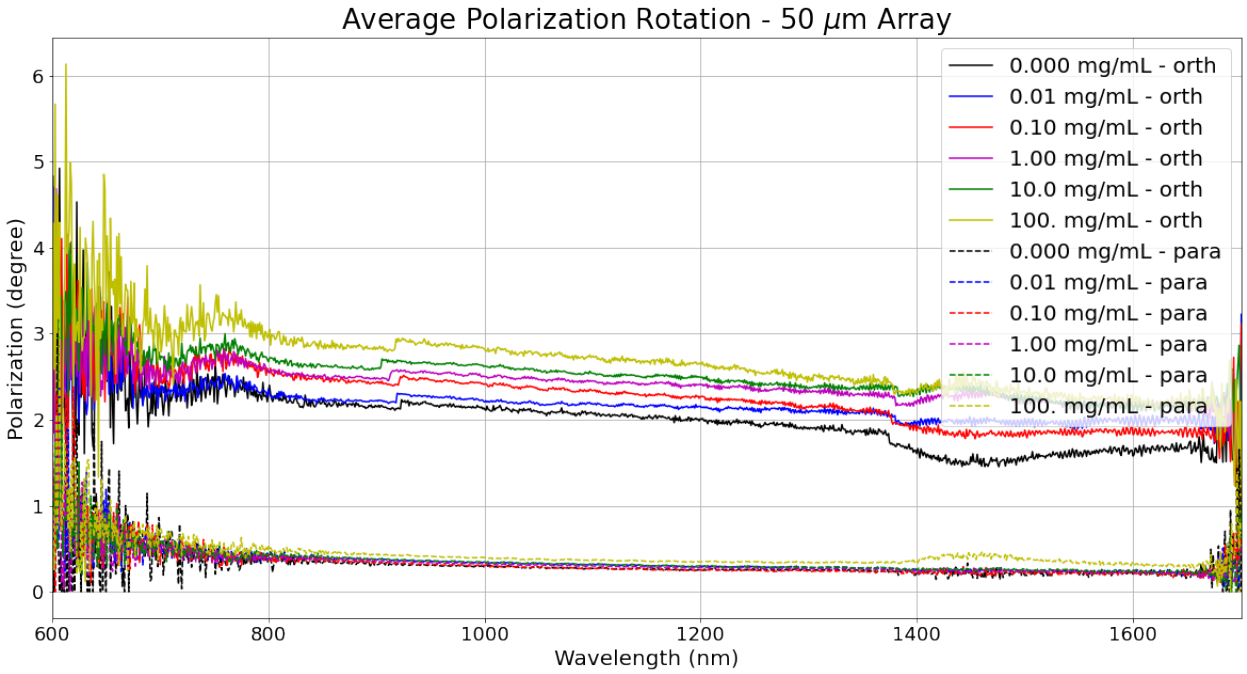

Figure 16: The average optical rotation of the 100-μm array. Both the orthogonal (solid) and parallel (dashed) source polarization data are shown.

Upon subtracting the optical rotation for the analyte containing no sucrose (DI water only, 0.000 mg/mL sucrose) to obtain the net rotation, the differences become starker. In the case of the E-field parallel to the wires (Figure 17), the net rotation is below 0.20°, and the rotation does not increase monotonically. In contrast, when the E-field is orthogonal to the wires (Figure 18), the net rotation ranges nearly a full degree, and increases monotonically between the

wavelengths of approximately 850 and 1350 nm. The net rotation data was truncated in the x-axis from 800 nm to 1500 nm, due to the saturation in the y-axis outside of that range.

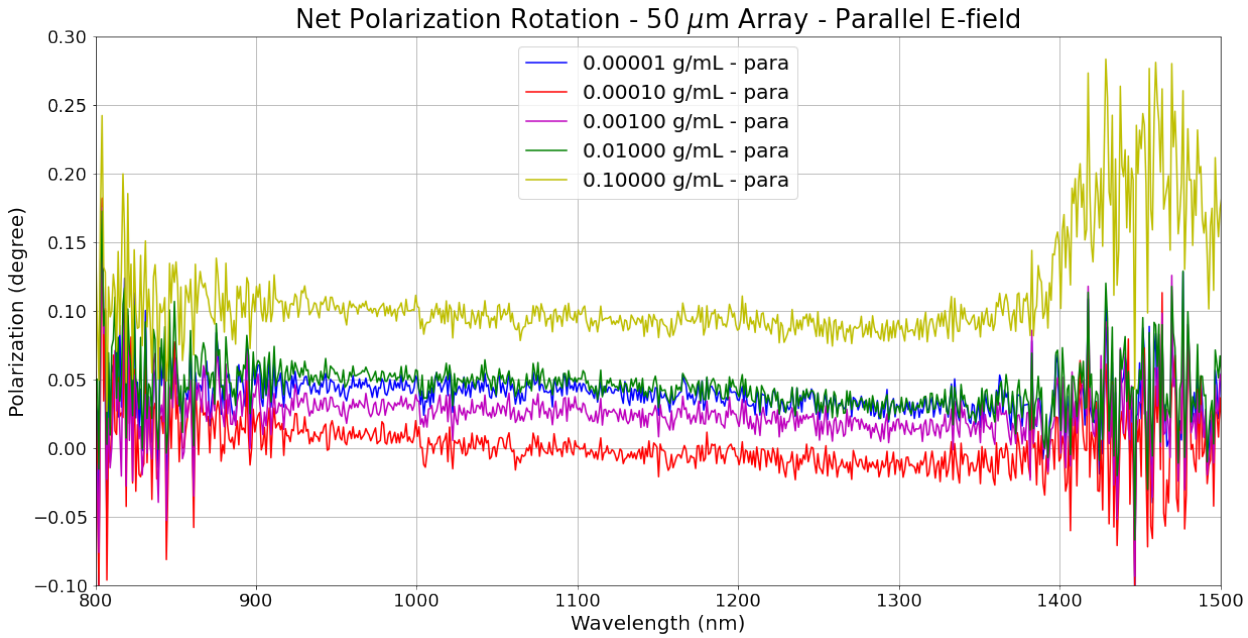

Figure 17: Net optical rotation of the different analyte concentrations for the source polarized parallel to the wires.

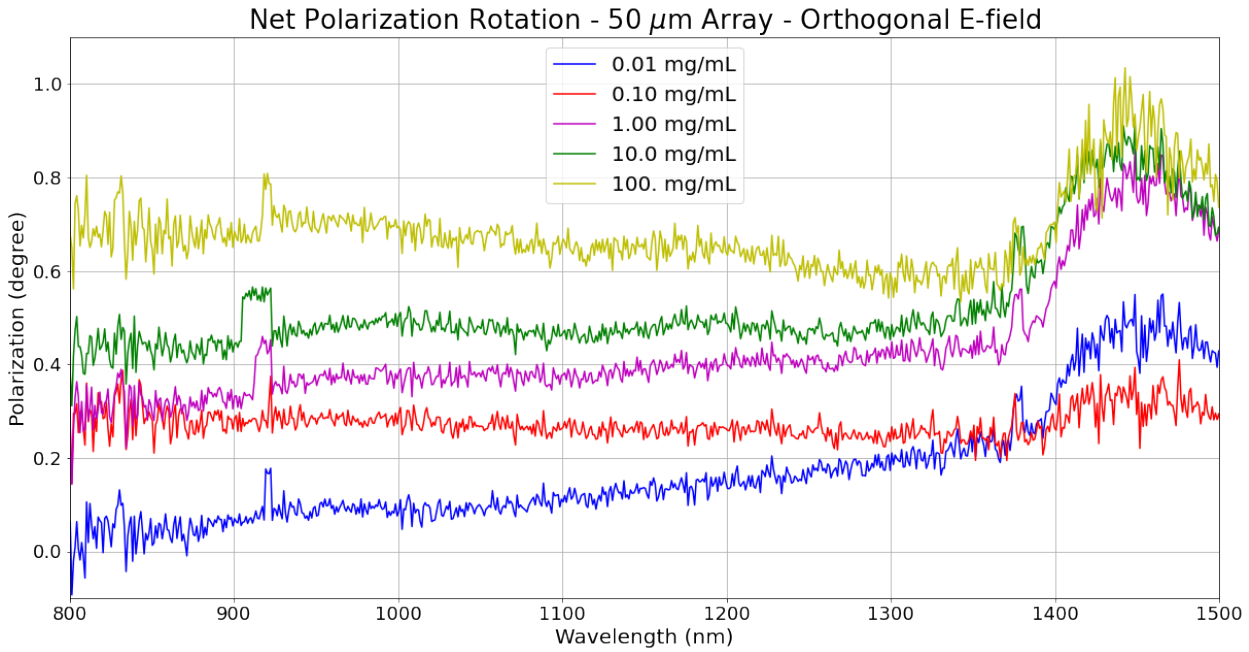

Figure 18: Net optical rotation of the different analyte concentrations for the source polarized orthogonal to the wires.

A closer look at the optical rotation at wavelengths of 1000 nm and 1200 nm (Figure 19) again confirm the previous observation, that the parallel polarization on the 50-µm array sample doesn't appear to induce much optical rotation. However, the orthogonal polarization does appear to induce an optical rotation that is concentration dependent, with small enough error that the different concentrations evaluated can be statistically distinguished from each other. This difference points to the possibility of an alignment of the sucrose molecules to the wire surface, when the E-field of the incident electromagnetic wave is aligned with the surface normal of the metallic core (which is perpendicular to the surface). The difference between the optical rotation between the 50-µm and the 100-µm array samples further suggests this surface effect, as the 50-µm array has a much higher surface to volume ratio between the microfiber wires and the microfluidic chamber. As a result, a greater proportion of molecules are at or near the surface of

the microfibers and subjected greater to both the surface electrical and magnetic fields, given the inverse dependence of field strength to distance (i.e., 1/r).

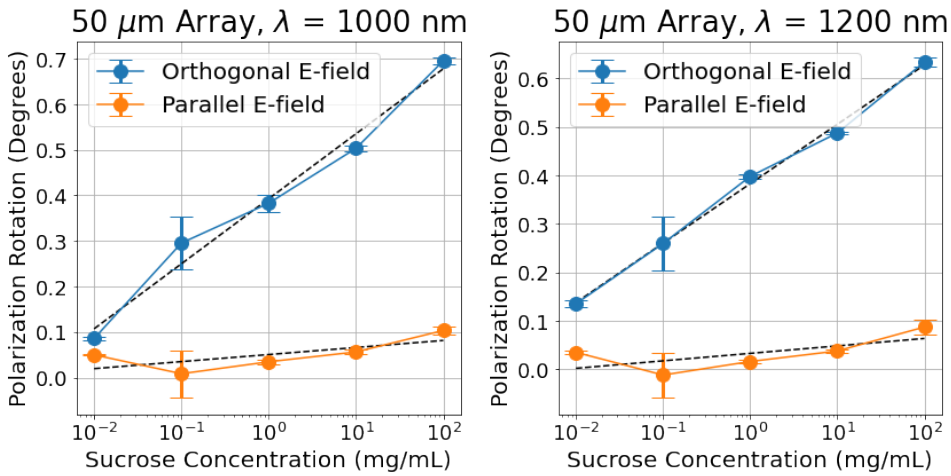

Figure 19: Average optical rotation of the 50-µm array sample with standard error bars, plotted as a function of analyte concentration, at wavelengths of 1000 nm [left] and 1200 nm [right].

The contribution of the microfiber arrays to the optical rotation amounts of the sucrose in general is significant. Based on Equation 3, the theoretical optical rotation of the different sucrose concentrations with the equivalent pathlength of the microfluidic chip (500 µm) are shown in Table 1. In comparison, the optical rotation observed in the 50-µm array microfluidic chip is greater in magnitude, with a low enough standard error at each tested analyte concentration to differentiate between them. The slope of the linear regression of the optical rotation as a function of the logarithmic value of the analyte concentration is shown in (Table 2).

Sucrose Concentration (mg/mL)			0.01	0.10	1.00	10.0	100.0
Theoretical Optical Rotation (degrees)			0.00000333	0.0000333	0.000333	0.00333	0.0333
Measured Optical Rotation (degrees)	50-µm Array Orthogonal Polarization	λ = 1000 nm	0.0858	0.2955	0.3828	0.5034	0.6956
		λ = 1200 nm	0.1349	0.2592	0.3956	0.4871	0.6337

Table 1: Theoretical optical rotation of sucrose solution, as a function of concentration and pathlength (500 µm), and the measured optical rotation of the 50-µm array sample with orthogonal source polarization.

Sample	Wavelength (nm)	Polarization	Linear Regression Slope
Control	1000	Parallel	-0.0793
		Orthogonal	0.0084
	1450	Parallel	-0.0050
		Orthogonal	-0.1792
100-µm Array	1000	Parallel	0.2135
		Orthogonal	0.1310
	1450	Parallel	0.2622
		Orthogonal	0.7444
50-µm Array	1000	Parallel	0.0155
		Orthogonal	0.1428
	1200	Parallel	0.0154
		Orthogonal	0.1225

Table 2: Slope of the linear regression line for each sample at different wavelengths and source polarization conditions. Slope units in degrees per logarithmic concentration (mg/mL).

3.2 – Wicking Effect

A demonstration of the wicking effect of the microfluidic chip was performed, for the 50-µm array sample. The frames from the video, as shown in Figure 20, demonstrate how the DI water colored with red dye is applied to the left of the microfluidic chip, and becomes readily wicked across the chip into the tissue paper that acts as a osmotic reservoir.

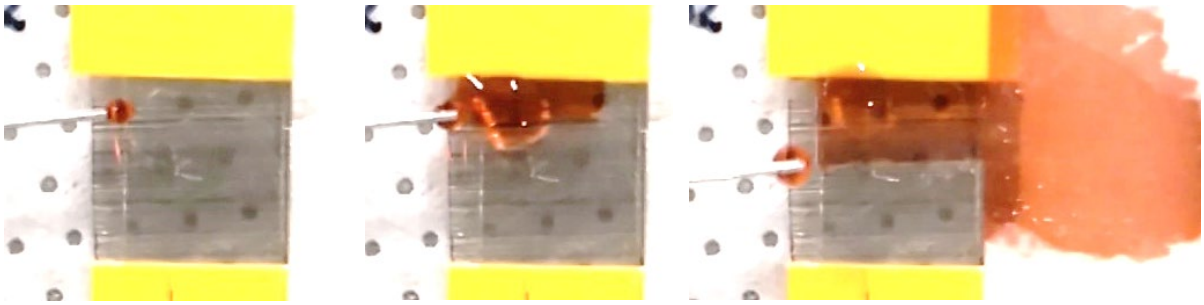

Figure 20: Frames from a video recording of the 50-µm array microfluidic chip wicking test. Beginning to end shown left to right. Note red dye DI water travelling from left to right.

This wicking effect is indicative of the potential sweat extraction and transport capabilities of a wearable platform that could be further developed on this feasibility study. As Laplace (capillary) pressure is inversely proportional to the channel width [28] (i.e. the microfiber array spacing in this system) and could potentially be actively tuned, there is an opportunity for further study and development that is accessible to both the array fabrication process as well as the sensing platform developed in this study.

Chapter 4: Conclusions

The optical rotation effect of the control and 100-µm spacing array samples are dominated by a material effect, causing a rotation of approximately 55° to 90°. This is most likely due to the stress-induced birefringence of the PETE polymer adhesive layers used in the fabrication. Also, the standard error of the data at each concentration suggests that the different concentrations cannot be statistically distinguished from each other for both the 100-µm array and control samples. However, as the center-to-center array spacing decreases to 50-µm, leading to both an increase in the volume- and surface-fraction of the ferromagnetic microfiber, there is a filtering effect observed that limits the optical rotation to under 4°. For the orthogonal source polarization, a clear monotonically increasing relationship between the optical rotation and the

logarithmic concentration of the analyte solution can be observed, with a low enough standard error that each tested concentration can be distinguished from each other. The slope of this relationship is 0.1428 and 0.1225 at wavelengths of 1000 nm and 1200 nm. The nominal polarization rotation for the 50-μm array sample at incidence orthogonal polarization is also several magnitudes greater than the theoretical optical rotation as an effect of just the sucrose solution, ranging from approximately 4 orders of magnitude at 0.01 mg/mL, decreasing to approximately one order of magnitude at 100.0 mg/mL.

As a proof-of-concept, this platform was successfully able to function as an optical sucrose solution concentration sensor, in the range of 0.01 to 100.0 mg/mL concentration, without the use of a chemical-enzyme interaction that is required for many current sensors. While a range of 0.01 to 0.10 mg/mL concentration would be theoretically enough to function as a sweat sensor, there are molecular differences between sucrose and glucose, the latter of which is the clinically relevant molecule and requires further characterization of the system. Sweat is also a more complex biofluid than a simple sucrose solution, with multiple other confounding molecules such as salts and other biological products. As such, the system needs to be assessed further with the addition of different molecules at different concentrations to develop a calibration method for a multi-variable space.

Further probing is also required into the combination effects of the composite between the microfiber wire array and the PETE polymer sheet, as to whether the observed optical rotation amplification effect requires the wires to be combined with a birefringent material to produce the observed effect. Different materials such as an annealed polymer (to remove strain-induced birefringence) should be utilized in constructing the microfluidic channel to isolate the contributions of each component. Additionally, different wire diameter sizes, array spacings, and

greater wavelengths should be evaluated. As the wire size and array spacing reach fractional dimensions of the test wavelengths, certain transverse wave-guiding modes could be utilized to add wavelength dependent sensing capabilities. Additionally, as the array spacing becomes too small to allow transmission-based sensing, various reflection modes should be considered, which could simplify the sensing mechanism for use as an adhesive patch system. The system could be further simplified with a more monochromic source, such as a light emitting diode or a laser coupled with chip-based sensors with polarization filters, removing the need for the cumbersome fiber coupling and spectrometer, and further allow the sensing system in a wearable ambulatory use case.

Several other tunable factors exist for the further development of this platform, including the wicking effect demonstrated in this work. This space can be further expanded by exploring the capabilities of the metallic core, as an electrically conductive medium that is susceptive to contactless actuation via inductive heating and magnetization.

In summary, the ferro-magnetic core/dielectric shell microfiber array system demonstrates promise as an optical sensing mechanism for the concentration of sucrose in the range of 0.01 to 100.0 mg/mL, and potentially other biomarkers of interest. In addition, its scalability, flexibility, active tunability, and both chemical and mechanical durability as a fiber-based system merits future study for its applications as a wearable biosensing system.

References

[1] American Diabetes Association, "Diagnosis and Classification of Diabetes Mellitus," *Diabetes Care,* 2010.

[2] International Diabetes Federation, "IDF Atlas 10th edition," *IDF Diabetes Atlas,* 2021.

[3] S. Coster, "Monitoring blood glucose control in diabetes mellitus: a systematic review," *Health Technol. Assess,* 2000.

[4] L. Welschen, "Self-monitoring of blood glucose in patients with type 2 diabetes who are not using insulin," *Diabetes Care,* 2005.

[5] L. Cark, "Electrode systems for continuous monitoring in cardiovascular surgery," *Ann. New York Acad. Sci.,* 1962.

[6] M. Guido Freckmann, "Measures of Accuracy for Continuous Glucose Monitoring and Blood Glucose Monitoring Devices," *Journal of Diabetes Science and Technology,* 2018.

[7] J. Moyer, "Correlation between sweat glucose and blood glucose in subjects with diabetes.".

[8] Z. Peng, "Blood glucose sensors and recent advances: A review," *Journal of Innovative Optical Health Sciences,* 2022.

[9] J. Wu, "A new generation of sensors for non-invasive blood glucose monitoring," *Am J Transl Res,* 2023.

[10] B. Cameron, "Development of an optical polarimeter for in-vivo glucose monitoring.," in *BiOS '99 International Biomedical Optics Symposium*, San Jose, CA, USA, 1999.

[11] C. Pirnstill, "In vivo glucose monitoring using dual-wavelength polarimetry to overcome corneal birefringence in the presence of motion," *Diabetes Technology & Therapeutics,* 2012.

[12] A. Szabo, "Theory of fluorescence depolarization in macromolecules and membranes," *The Journal of chemical physics,* 1984.

[13] A. Bandodkar, "Tatto-based noninvasive glucose monitoring: a proof-of-concept study," *Anal. Chem,* 2015.

[14] H. Lee, "Enzyme-based glucose sensor: from invasive to wearble device," *Adv. Healthcare Mater.,* 2018.

[15] N. Oliver, "Glucose sensors: a review of current and emerging technology," *Diabetic Medicine,* 2009.

[16] R. Nave, "HyperPhysics," Georgia State University, 2000. [Online]. Available: http://hyperphysics.phy-astr.gsu.edu/hbase/phyopt/polclas.html. [Accessed 15 4 2024].

[17] Chemical Education Division, "Chirality and Optical Activity," Perdue University Dept. of Chem. Ed., 1979. [Online]. Available: https://chemed.chem.purdue.edu/genchem/topicreview/bp/1organic/chirality.html. [Accessed 15 4 2024].

[18] Y. Xu, "Specific detection of glucose by an optical weak measurement sensor," *Biomedical Optics Express,* 2021.

[19] "Lab Cat," 27 1 2009. [Online]. Available: https://cdavies.wordpress.com/2009/01/27/simple-sugars-fructose-glucose-and-sucrose/. [Accessed 15 4 2024].

[20] F. Capolino, Theory and Phenomena of Metamaterials, CRC Press, 2017.

[21] A. Chiappini, "Photonic Crystal Stimuli-Responsive Chromatic Sensors: A Short Review," *MDPI Micromachines,* 2020.

[22] F. Wu, "Sensitive sucrose biosensors with high Q factors empowered by quasi-bound states in the continuum in compound grating waveguide structures," *Physics,* 2023.

[23] S. Agarwal, "Metamaterial based sucrose detection sensor using transmission spectroscopy," *Optik,* 2020.

[24] Q. Zhi, "Fe2AlB2: A novel ferromagnetic material with superior electromagnetic wave absorption performance," *Ceramics International,* 2023.

[25] R. Naaman, "Chiral molecules-ferromagnetic interfaces, an approach towards spin controlled interactions," *Appl. Phys Lett.,* 2019.

[26] S. Min, "Polarimetric Study of an Embeddable, Flexible, Textile-Compatible Ferromagnetic Microfiber Platform.," in *Materials Research Society Fall Meeting and Exhibit*, Boston, 2023.

[27] Z. Zhou, "Strain-optical behavior of polyethylene terephthalate film during uniaxial stretching investigated by Mueller matrix ellipsometry," *Polymer,* 2019.

[28] D. Junker, Capillary Microfluidic Systems for Bio/Chemistry, 2002.

[29] D. Li, "An Optical Chiral Sensor Based on Weak Measurement for the Real-Time Monitoring of Sucrose Hydrolysis," *MDPI Sensors,* 2021.

[30] W. Gao, "Fully integrated wearable sensor arrays for multiplexed in situ perspiration analysis," *Nature,* 2016.

Appendix A – Python Code

[1]:
```
# Import required packages
import matplotlib.pyplot as plt
import numpy as np
import time
# %config InlineBackend.figure_format = 'svg' # this is key to improving plot resolution
```

[2]:
```
# Get TinkerForge components
from tinkerforge.ip_connection import IPConnection
from tinkerforge.bricklet_silent_stepper_v2 import BrickletSilentStepperV2
```

[3]:
```
HOST = "localhost"
PORT = 4223
UID_Screw = "26Nm"
UID_Roller = "26Na"
```

[4]:
```
ipcon = IPConnection() # Create IP connection

lin_screw = BrickletSilentStepperV2(UID_Screw, ipcon) # Create device object
roller = BrickletSilentStepperV2(UID_Roller, ipcon) # Create device object

ipcon.connect(HOST, PORT) # Connect to brickd
# Don't use device before ipcon is connected
time.sleep(0.2)
```

[5]:
```
lin_screw.set_motor_current(400) # 400 mA
lin_screw.set_step_configuration(lin_screw.STEP_RESOLUTION_256, True) # 256 micro-steps per macro-step (interpolated between each of the 200 macro-steps per rev)

roller.set_motor_current(400) # 400 mA
roller.set_step_configuration(roller.STEP_RESOLUTION_256, True) # 256 micro-steps per macro-step (interpolated between each of the 200 macro-steps per rev)
```

[6]:
```
gear = 26. + (103./121.)    # gear-box ratio
# step angle w/o gearbox = 1.80 deg - 200 steps/rev

macro_rev = 200. * gear       # macro-steps per revolution
micro_rev = 256. * macro_rev  # micro-steps per revolution
print(micro_rev)
```

```
1374783.4710743802
```

[7]:
```
windings = 200.            # number of windings

fiber_dia = 27.            # um - micrometer measurement
# 20 um core, 10 um shell?
# minimum winding spacing = 40 um center to center
gap = 23.                   # um - edge to edge spacing

spacing = gap+fiber_dia    # um - center to center spacing
# 1 spacing required for 1 revolution of roller
print("ctc spacing: " + str(spacing) + " um")

length = windings * (spacing)
print("total width: " + str(length) + " um")
```

```
ctc spacing: 50.0 um
total width: 10000.0 um
```

[8]:
```
# Lead screw m8x1.5
# 1 micro_rev = 1.5 mm = 1500 um

per_rev = 1500. / spacing       # wire spacings per rev of lead screw
clicks = micro_rev / per_rev    # micro-steps per spacing
print(clicks)
```

```
45826.11570247934
```

[9]:
```
roll_speed = 60000            # set roller speed - micro-step per second
roll_accel = round(roll_speed)

roller.set_max_velocity(roll_speed)
roller.set_speed_ramping(roll_accel, roll_accel)

lin_speed = round(roll_speed/per_rev) # set linear screw speed - micro-step per second
print(lin_speed)

lin_accel = round(lin_speed)
lin_screw.set_max_velocity(lin_speed)
lin_screw.set_speed_ramping(lin_accel, lin_accel)
```

```
2000
```

[10]:
```
lin_screw.set_enabled(True)    # Enable motor power
roller.set_enabled(True)      # Enable motor power
```

[11]:
```
print(int(windings))
```

```
200
```

[ ]:
```
# drive roller backward (negative steps) and lin_screw forward (positive steps) to wind

## all windings in one go
roller.set_steps(-round(micro_rev)*windings) # Drive steps backward to make 1 roller rev
lin_screw.set_steps(round(clicks)*windings) # Drive steps forward to make 1 fiber spacing
input("Press any key to exit\n")
time.sleep(0.4)


## one winding at a time
# i = 0
# for i in range(int(windings)):
#     roller.set_steps(-round(micro_rev)) # Drive steps backward to make 1 roller rev
#     lin_screw.set_steps(round(clicks)) # Drive steps forward to make 1 fiber spacing
#     input("Press key to exit\n")
#     time.sleep(30)
#     i += 1
```

[15]:
```
roller.stop() # Request motor stop
lin_screw.stop()
time.sleep(0.4) # Wait for motor to actually stop
```

[39]:
```
roller.set_enabled(False) # Disable motor power
lin_screw.set_enabled(False) # Disable motor power


# Disconnect from Tinkerforge
ipcon.disconnect()
```

Appendix B – Source Spectra

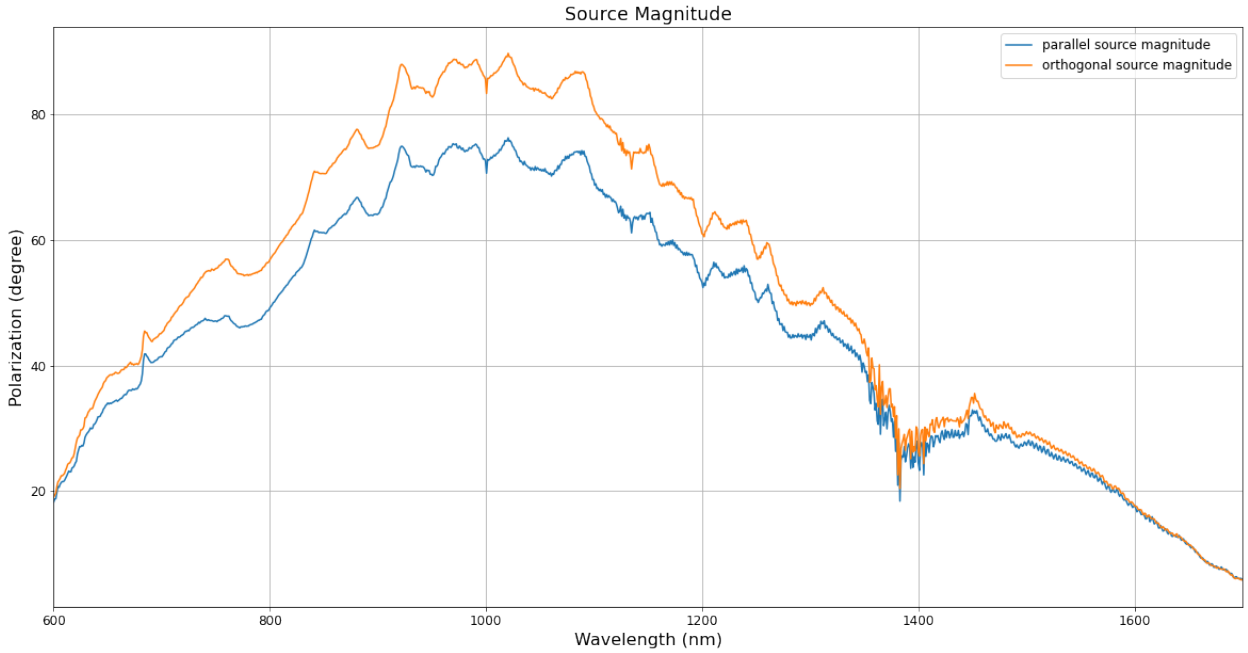

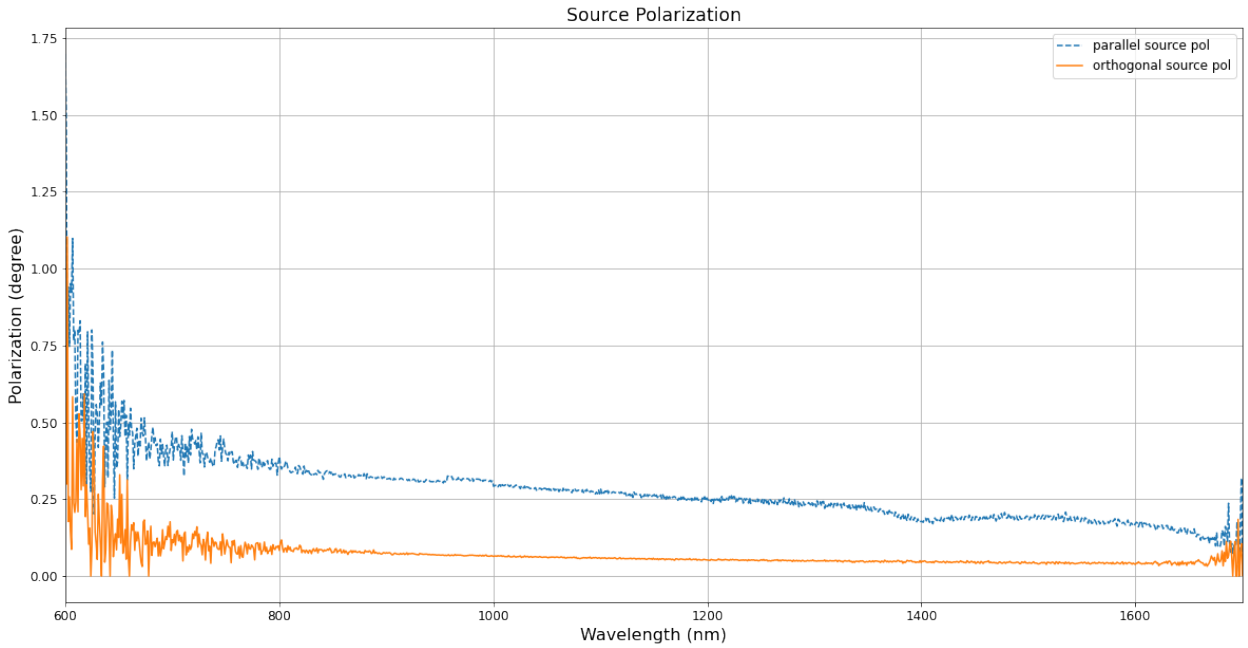

Appendix C – Control Spectra

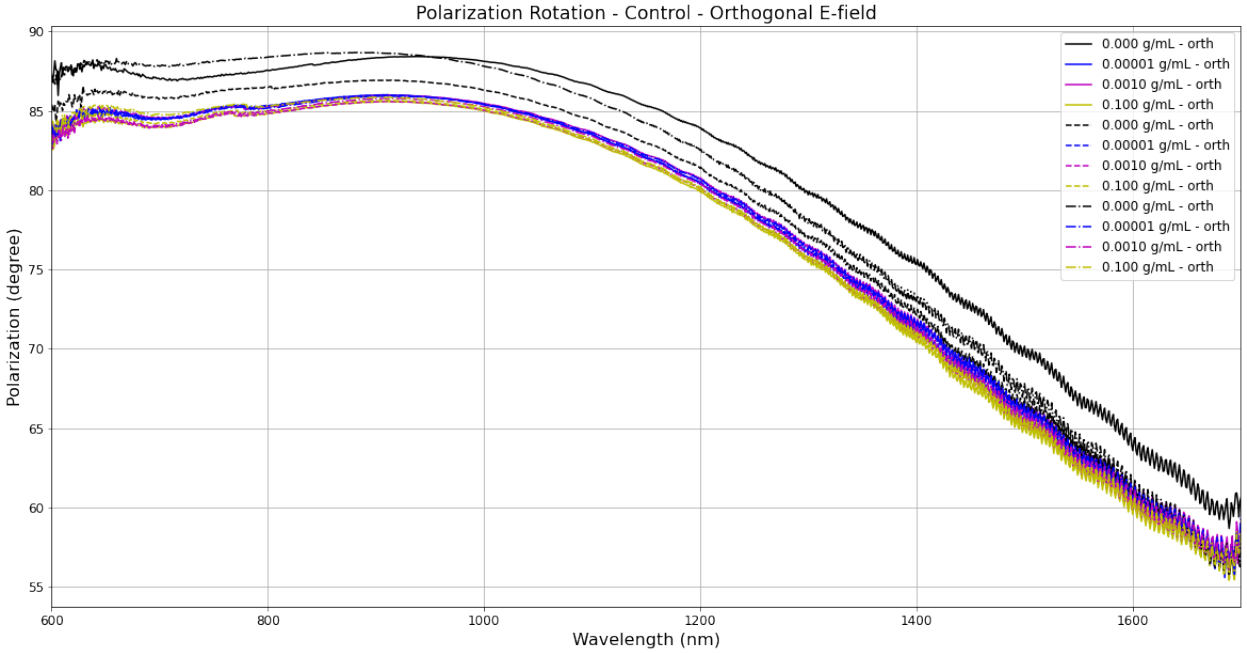

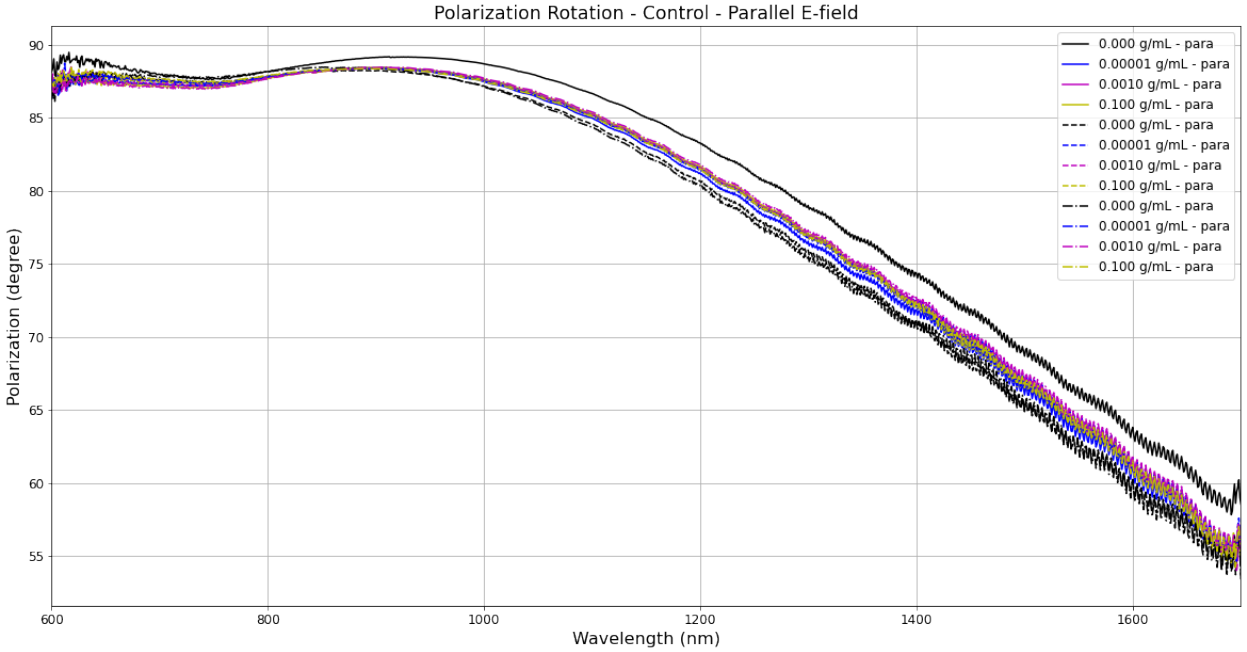

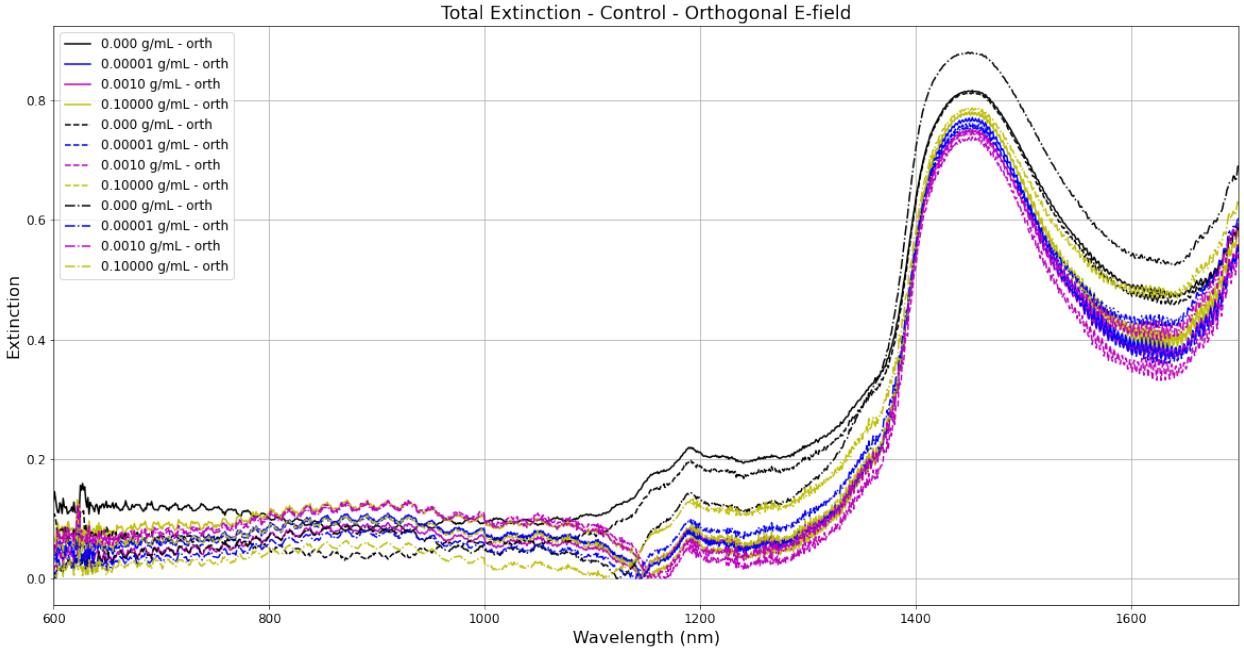
Total Extinction - Control - Orthogonal E-field
0.000 g/mL - orth
0.00001 g/mL - orth
0.0010 g/mL - orth
0.10000 g/mL - orth
0.000 g/mL - orth
0.00001 g/mL - orth
0.0010 g/mL - orth
0.10000 g/mL - orth
0.000 g/mL - orth
0.00001 g/mL - orth
0.0010 g/mL - orth
0.10000 g/mL - orth
Extinction
Wavelength (nm)

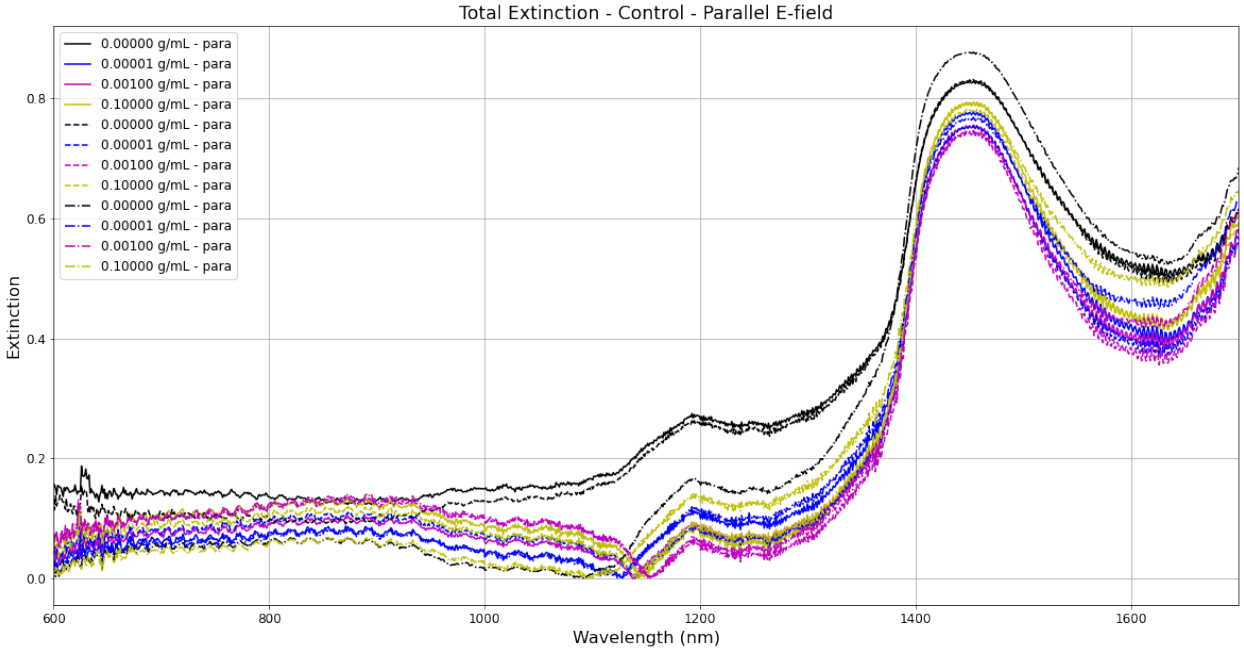
Total Extinction - Control - Parallel E-field
0.00000 g/mL - para
0.00001 g/mL - para
0.00100 g/mL - para
0.10000 g/mL - para
0.00000 g/mL - para
0.00001 g/mL - para
0.00100 g/mL - para
0.10000 g/mL - para
0.00000 g/mL - para
0.00001 g/mL - para
0.00100 g/mL - para
0.10000 g/mL - para
Extinction
Wavelength (nm)

Appendix C – 100-µm Array Spectra

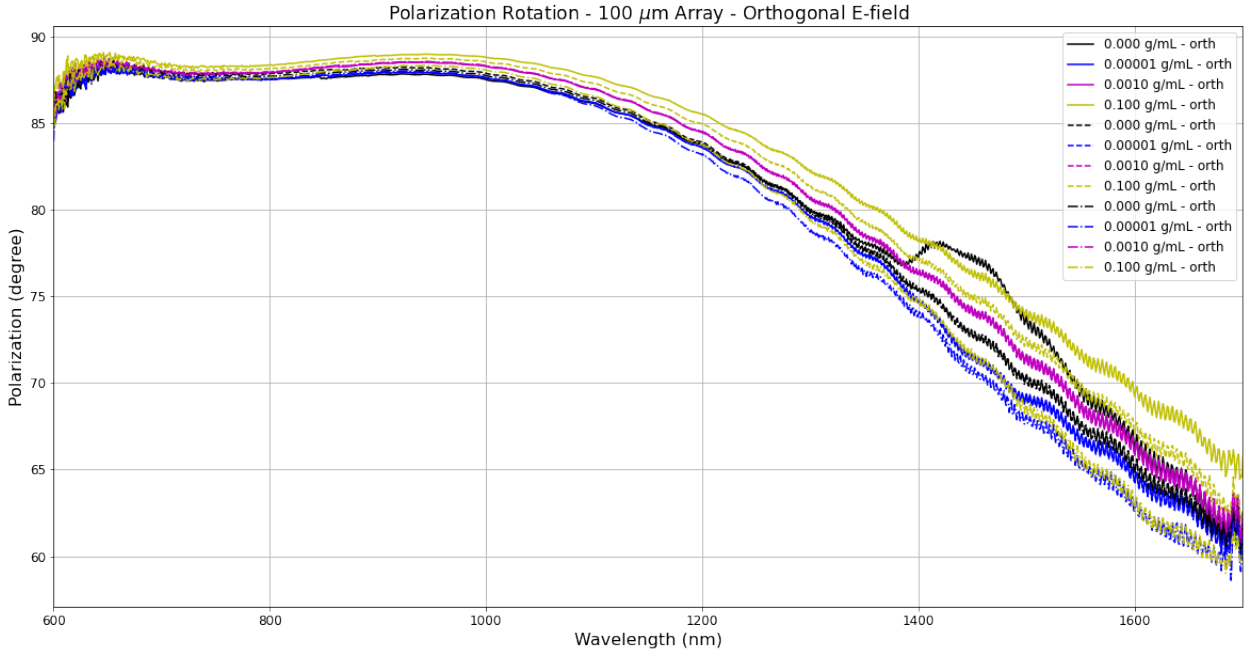

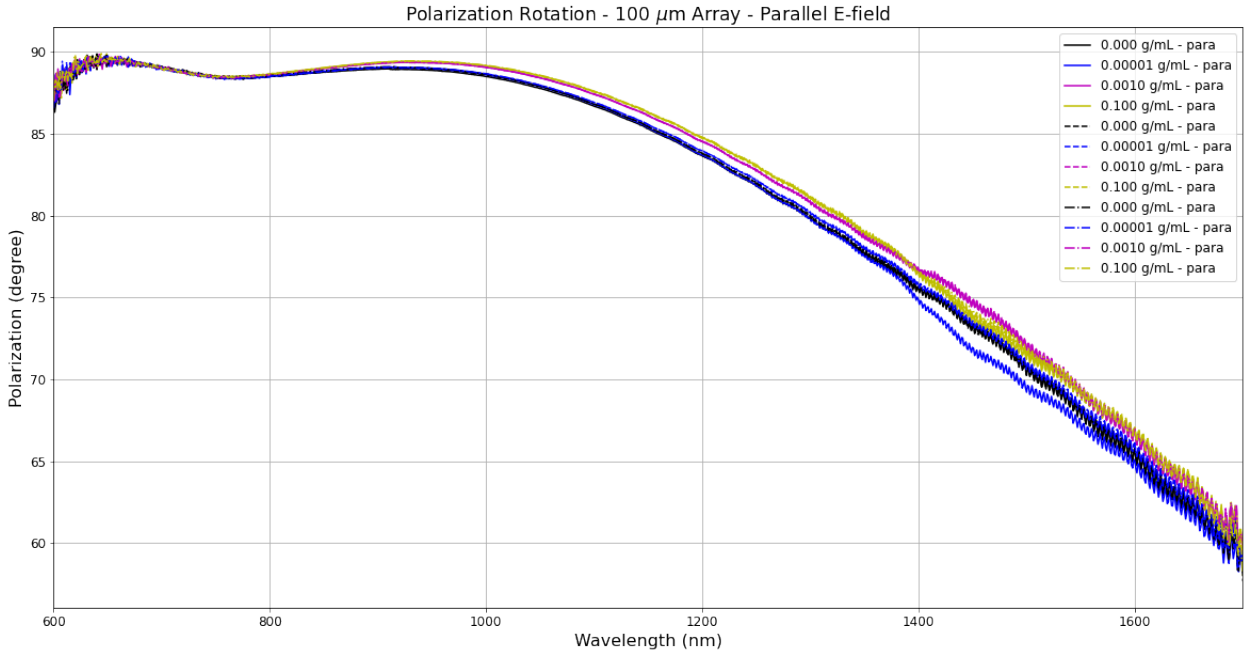

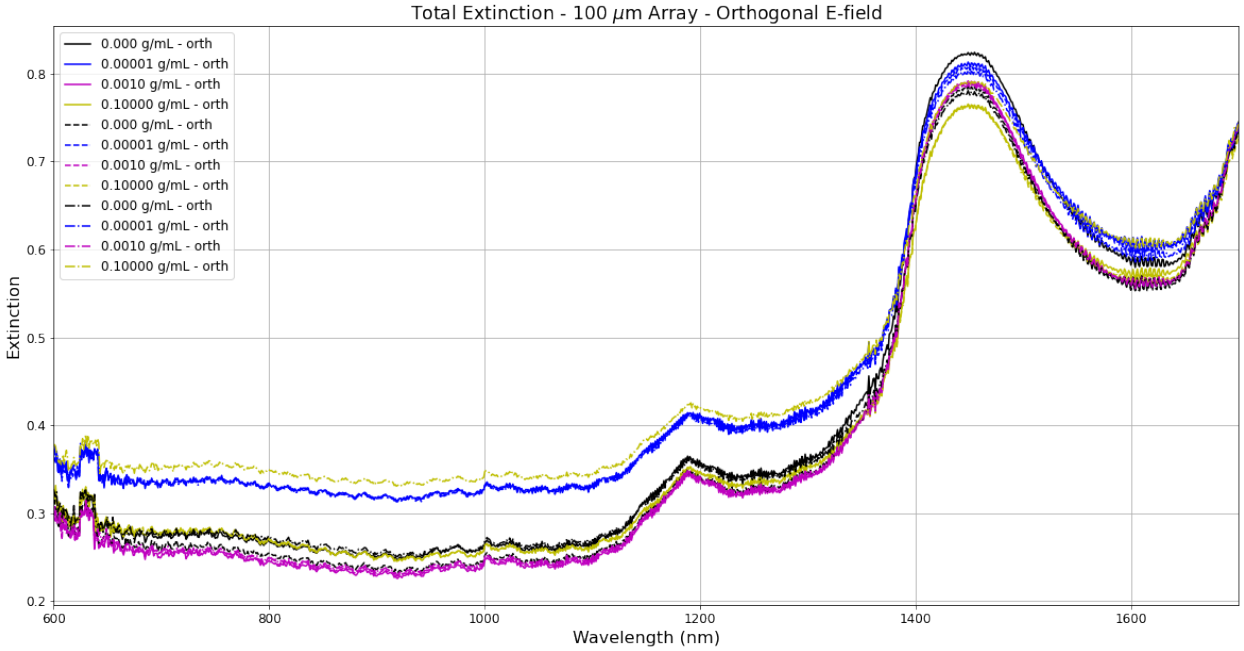
Total Extinction - 100 μm Array - Orthogonal E-field
0.000 g/mL - orth
0.00001 g/mL - orth
0.0010 g/mL - orth
0.10000 g/mL - orth
0.000 g/mL - orth
0.00001 g/mL - orth
0.0010 g/mL - orth
0.10000 g/mL - orth
0.000 g/mL - orth
0.00001 g/mL - orth
0.0010 g/mL - orth
0.10000 g/mL - orth
Extinction
Wavelength (nm)

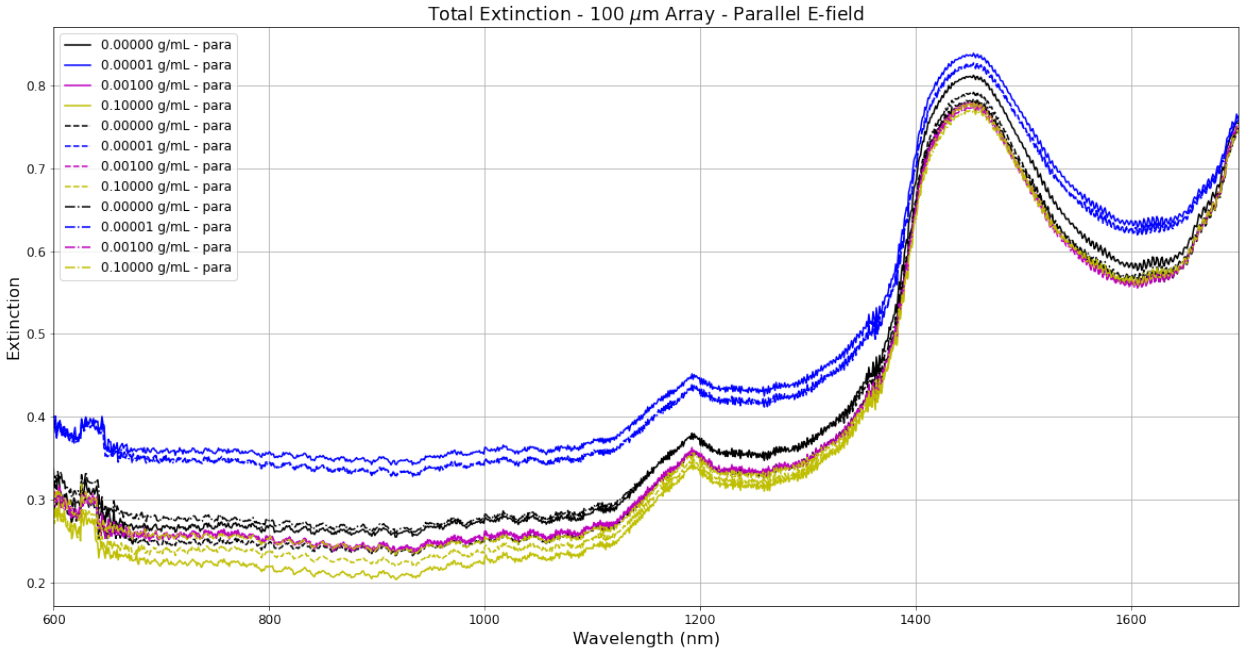
Total Extinction - 100 μm Array - Parallel E-field
0.00000 g/mL - para
0.00001 g/mL - para
0.00100 g/mL - para
0.10000 g/mL - para
0.00000 g/mL - para
0.00001 g/mL - para
0.00100 g/mL - para
0.10000 g/mL - para
0.00000 g/mL - para
0.00001 g/mL - para
0.00100 g/mL - para
0.10000 g/mL - para
Extinction
Wavelength (nm)

Appendix D – 50-µm Array Spectra

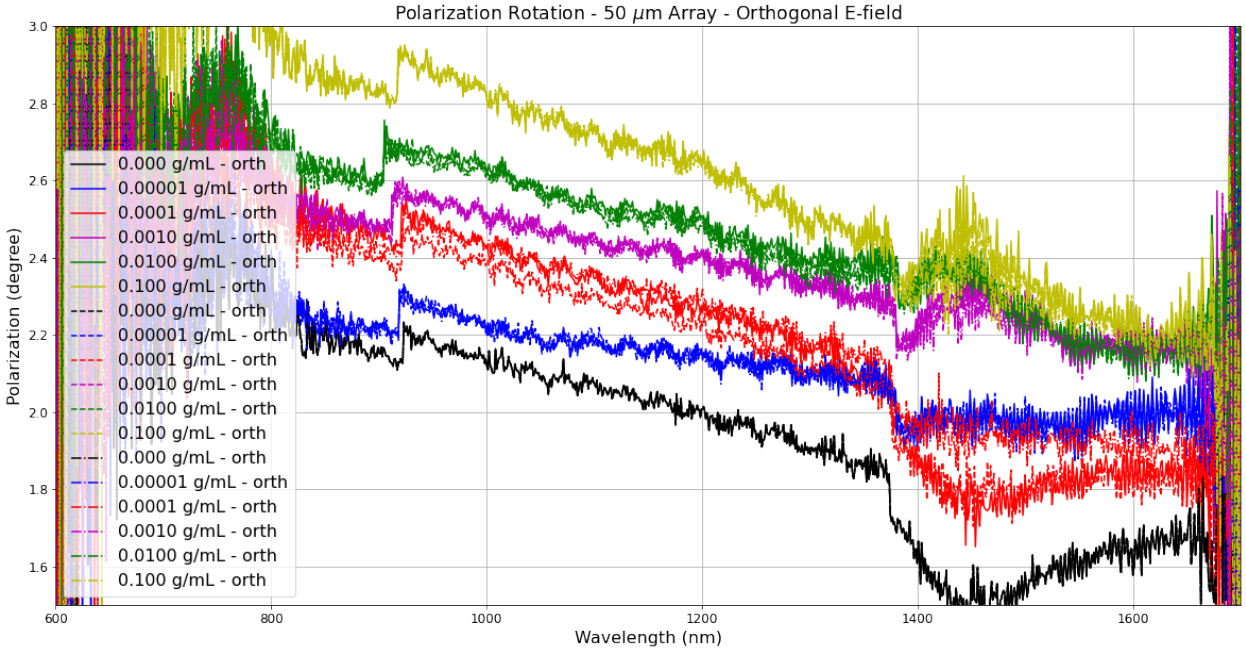

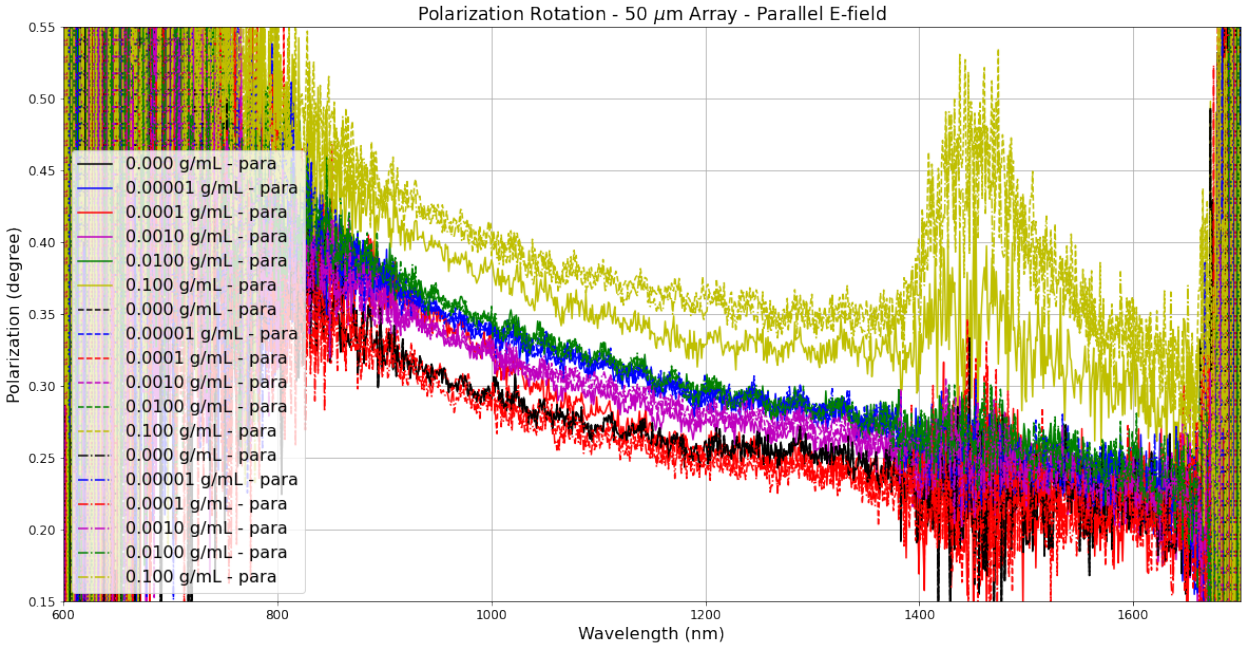

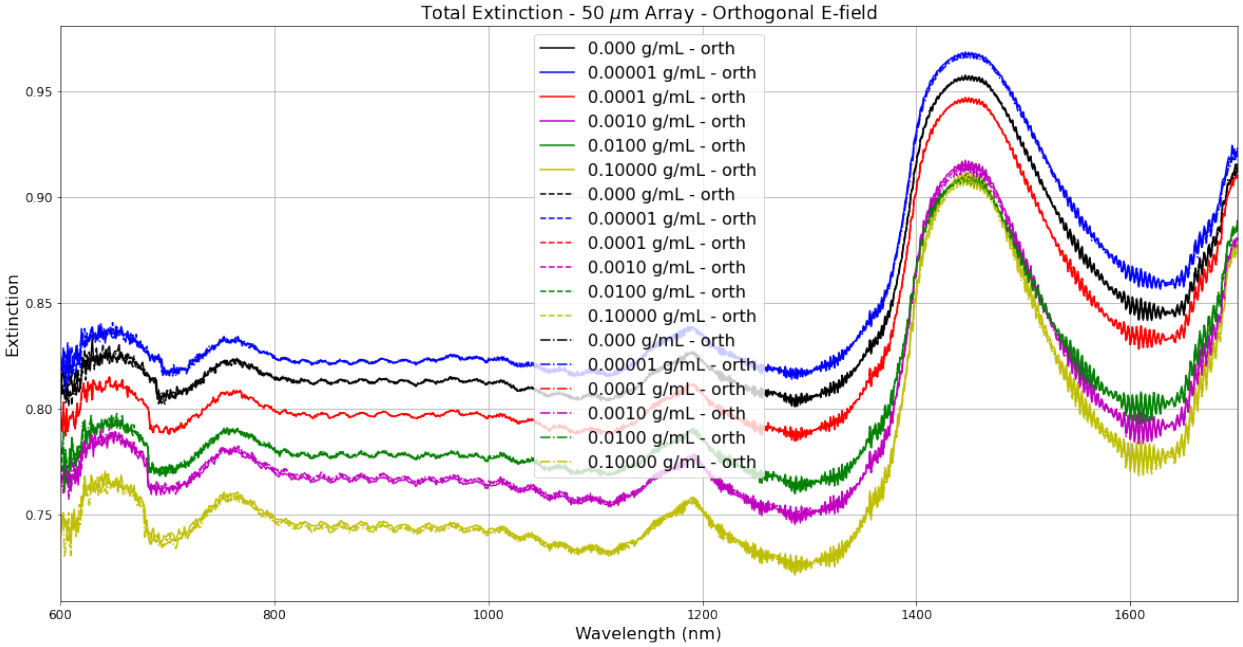
Total Extinction - 50 μm Array - Orthogonal E-field
0.000 g/mL - orth
0.00001 g/mL - orth
0.0001 g/mL - orth
0.0010 g/mL - orth
0.0100 g/mL - orth
0.10000 g/mL - orth
0.000 g/mL - orth
0.00001 g/mL - orth
0.0001 g/mL - orth
0.0010 g/mL - orth
0.0100 g/mL - orth
0.10000 g/mL - orth
0.000 g/mL - orth
0.00001 g/mL - orth
0.0001 g/mL - orth
0.0010 g/mL - orth
0.0100 g/mL - orth
0.10000 g/mL - orth
Extinction
Wavelength (nm)

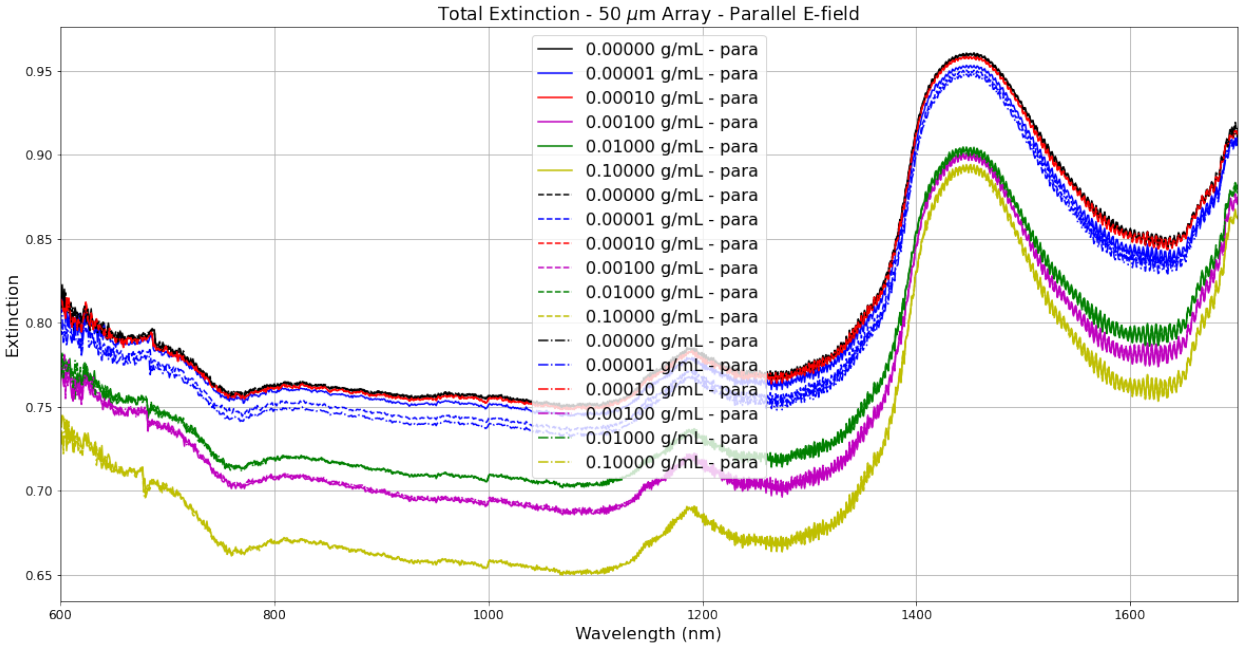
Total Extinction - 50 μm Array - Parallel E-field
0.00000 g/mL - para
0.00001 g/mL - para
0.00010 g/mL - para
0.00100 g/mL - para
0.01000 g/mL - para
0.10000 g/mL - para
0.00000 g/mL - para
0.00001 g/mL - para
0.00010 g/mL - para
0.00100 g/mL - para
0.01000 g/mL - para
0.10000 g/mL - para
0.00000 g/mL - para
0.00001 g/mL - para
0.00010 g/mL - para
0.00100 g/mL - para
0.01000 g/mL - para
0.10000 g/mL - para
Extinction
Wavelength (nm)